

Review article

Multifaceted nature of defect tolerance in halide perovskites and emerging semiconductors

Irea Mosquera-Lois^{1,†}, Yi-Teng Huang^{2,†}, Hugh Lohan^{2,1,†}, Junzhi Ye², Aron Walsh^{1,*} and Robert L. Z. Hoye^{2,*}

¹ Department of Materials, Imperial College London, Exhibition Road, London SW1 2AZ, United Kingdom

² Inorganic Chemistry Laboratory, Department of Chemistry, University of Oxford, South Parks Road, Oxford OX1 3QR, United Kingdom

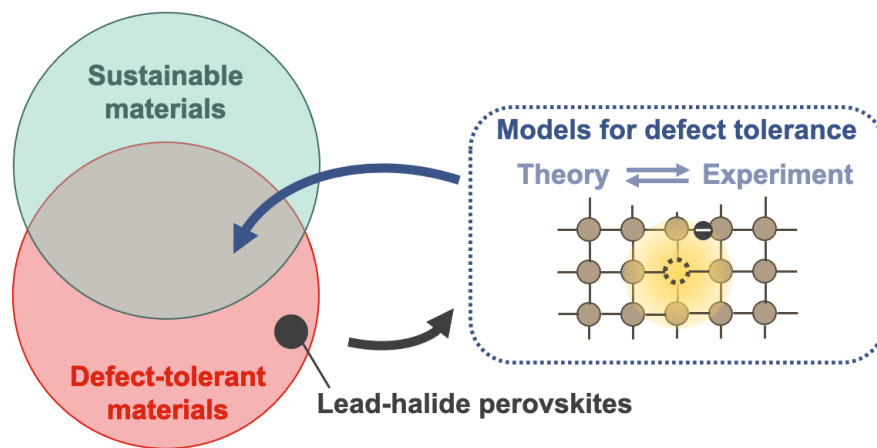
† These authors contributed equally

* e-mail: a.walsh@imperial.ac.uk (A.W.), robert.hoye@chem.ox.ac.uk (R. L. Z. H.)

Abstract

Lead-halide perovskites (LHPs) have shot to prominence as efficient energy conversion materials that can be processed using cost-effective fabrication methods. A widely-quoted reason for their exceptional performance is their ability to tolerate defects, enabling long charge-carrier lifetimes despite high defect densities. Realizing defect tolerance in broader classes of materials would have a substantial impact on the semiconductor industry. Significant effort has been made over the past decade to unravel the underlying origins of defect tolerance to design stable alternatives to LHPs comprised of nontoxic elements. However, it has become

clear that understanding defect tolerance in LHPs is far from straightforward. This review discusses the models proposed for defect tolerance in halide perovskites, evaluating the experimental and theoretical support for these models, as well as their limitations. We cover attempts to apply these models to identify materials beyond the lead-halide system that could also exhibit defect tolerance, and the successes and pitfalls encountered over the past decade. Finally, a discussion is made of some of the important missing pieces of information required for a deeper understanding and predictive models that enable the inverse design of defect tolerant semiconductors.



Introduction

Semiconductors that harvest light to produce clean electricity^{1,2}, or clean fuels and chemicals³⁻⁵, without emitting any greenhouse gases are becoming increasingly important for enabling society's transition to net-zero carbon dioxide equivalent (CO₂eq) emissions. The deployment of these technologies benefits from cost-effective manufacturing methods, but this typically leads to a compromise in performance because of the deleterious role played by defects¹. Defects in semiconductors lower performance by causing irreversible losses in energy (refer to Box 1), as well as limiting the transport of charge-carriers. The effects of defects have traditionally been mitigated by minimizing their presence through careful materials growth and passivation^{1,2,6,7}. But over the past decade, lead-halide perovskites (LHPs) have proven to be

an exception, rapidly rising in performance in photovoltaics (PVs; Fig. 1a), which harvest light to produce clean electricity. The most efficient LHP PV devices are made using simple solution processing or evaporation methods, are polycrystalline, and the absorber layer is processed at temperatures up to only 150 °C^{8,9}. By contrast, the most efficient Si PVs are made using capital-intensive equipment, are single crystalline, and processed at >1000 °C, and yet the certified record light-to-electricity power conversion efficiencies (PCEs) are very similar (27.3% for Si PVs, and 26.5% for LHP PVs at present)^{8,9,10}. The ability to achieve efficient LHPs using standard laboratory equipment has engaged a large global community, such that the cycles of learning required to reach the performance of single-crystalline Si (c-Si) PVs has taken a significantly shorter period of time (Fig. 1a vs. b).

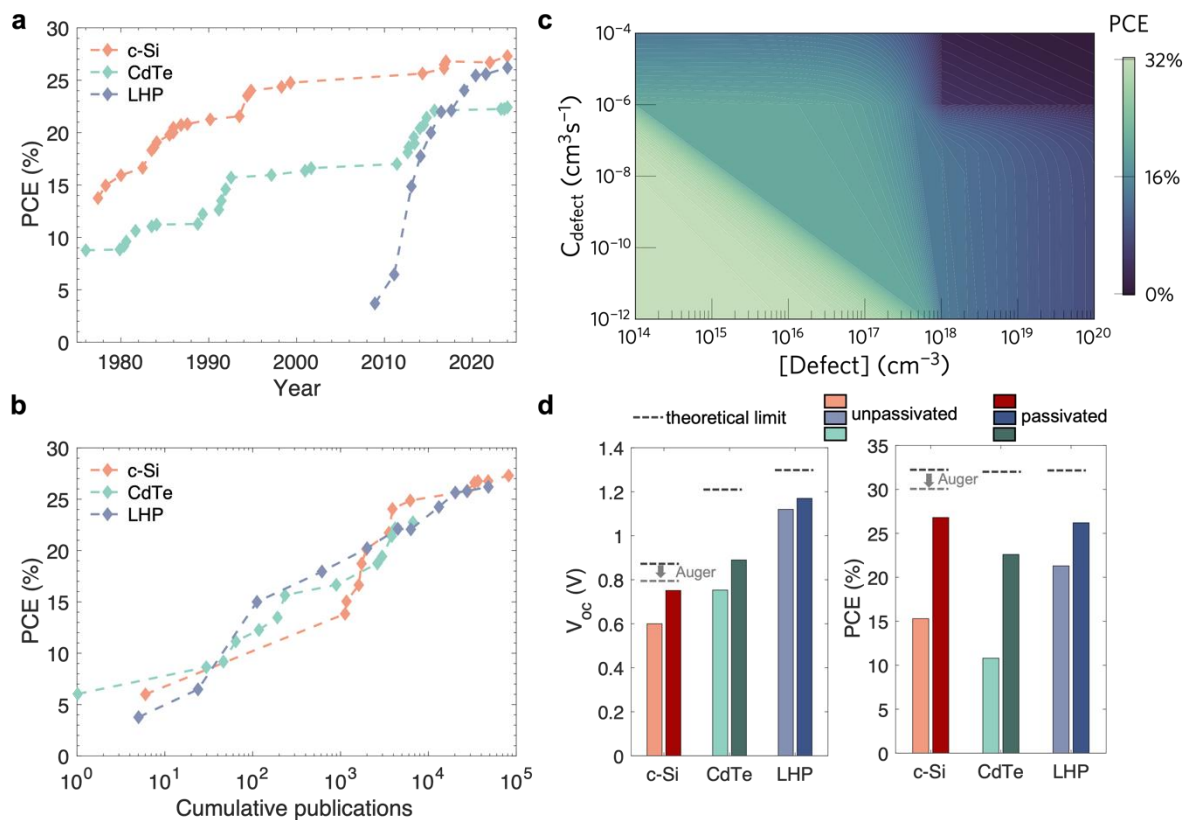


Fig. 1 | Impact of defect tolerance on the performance of solar absorbers. Comparison of the learning rate of lead-halide perovskite (LHP) *versus* crystalline silicon (c-Si) and cadmium telluride (CdTe) photovoltaics, with respect to **a**, development time and **b**, cumulative number of publications^{9,11-14}, which can be considered as a proxy for the level of effort. **c**, Map of the theoretical maximum power conversion efficiency of materials in PVs (PCE), depending on

the capture coefficient (C_{defect}) and concentration of defects. **d**, Loss in open-circuit voltage (V_{OC}) and power conversion efficiency of unpassivated and optimally passivated LHP, c-Si and CdTe photovoltaic devices compared to the radiative limit.

This unusual high-performance of LHPs has largely been attributed to defect tolerance, where high PCEs are achievable in solar cells despite a high defect density by primarily forming defects with low capture coefficients (Fig. 1c)^{6,7,15–18}. Indeed, PVs based on polycrystalline LHP thin films can achieve 21.2% PCE without any dedicated efforts to intentionally passivate defects in the bulk of the perovskite layer or at interfaces¹⁹, reaching 69% of the theoretical limit (Fig. 1d)^{19,20}. By contrast, polycrystalline Si PVs could only reach ~17% PCE without significant interface passivation (Fig. 1d)^{21–23}. If we compare LHPs with another polycrystalline direct-bandgap material, CdTe PVs could only reach ~10% PCE without passivation^{24,14}, while the optimally passivated devices are at only 70% of the theoretical limit—in contrast with 80% for passivated LHPs (Fig. 1d). Even in the most efficient LHP PVs, the defect density (10^{13} – 10^{17} cm⁻³)^{25–28} is orders of magnitude larger than in optimized single crystalline Si ($<10^{11}$ cm⁻³)²⁹.

Defect tolerance in solar absorbers was discussed over 20 years ago by Zhang *et al.* to account for the surprisingly high efficiency of CuInSe₂ despite hosting extraordinarily high concentrations of native defects on the order of ~1%³⁰. In this case, defect tolerance arises because the deep indium on copper antisites ($\text{In}_{\text{Cu}}^{2+}$) and copper vacancies (V_{Cu}^-) combine to form benign complexes ($2V_{\text{Cu}}^- + \text{In}_{\text{Cu}}^{2+}$) that can order to form new crystallographic phases³⁰. But for LHPs, a wide range of models have been put forward to account for their tolerance to point defects, which draw upon electronic and structural factors^{31–33}. More recently, the concept of defect tolerance has been extended by considering that the dynamic disorder of LHPs results in significant energetic fluctuations in trap levels, by as much as 1 eV on a picosecond

timescale³⁴, raising the question of how traps can then be considered shallow or deep. Defect spectroscopy in LHPs is also complicated by contributions from ionic and electronic processes that are difficult to disentangle³⁵. Deep-level transient spectroscopy measurements have indicated deep traps to be present^{36,37}. Some of these defects are relatively benign with small capture cross-sections ($\sim 10^{-15} \text{ cm}^2$)^{36,37}, while other works have identified more harmful defects with larger capture cross-sections $\sim 10^{-12} \text{ cm}^2$ ³⁷. On the other hand, using positron annihilation lifetime spectroscopy on methylammonium lead iodide (MAPbI₃), it was confirmed that positively charged defects (*e.g.*, V_{I}^+) have negligible trapping rates and are benign, whereas negatively charged lead vacancies in this perovskite were identified and found to act as recombination centres³⁸. The concentration of these V_{Pb}^{2-} was estimated to be high, in the range of 10^{15} – 10^{17} cm^{-3} ³⁸. Despite this, the non-radiative recombination coefficient reported for MAPbI₃ (1.4 – $1.5 \times 10^7 \text{ s}^{-1}$) is similar to established inorganic semiconductors, such as c-Si (0.1 – $2.5 \times 10^7 \text{ s}^{-1}$) and GaN (0.1 – $1.0 \times 10^7 \text{ s}^{-1}$)³⁹.

The field has therefore reached a critical juncture, where it is important to bring together the past decade of experimental and computational work to evaluate the multifaceted nature of defect tolerance in LHPs. This review begins by discussing the definition of defect tolerance, which is inconsistent between communities because of the different ways in which defects are probed. Next, we evaluate the models put forward for defect tolerance, discussing the evidence for and against these models. We balance out the review with a discussion of efforts to generalize defect tolerance beyond LHPs, which can lead to the discovery of efficient, cost-effective solar absorbers that overcome the stability and toxicity limitations of halide perovskites. We discuss the strategies that have been adopted, as well as the successes and challenges found among the materials investigated. Finally, we discuss some of the important questions that need to be addressed to move forward towards a consolidated view of defect

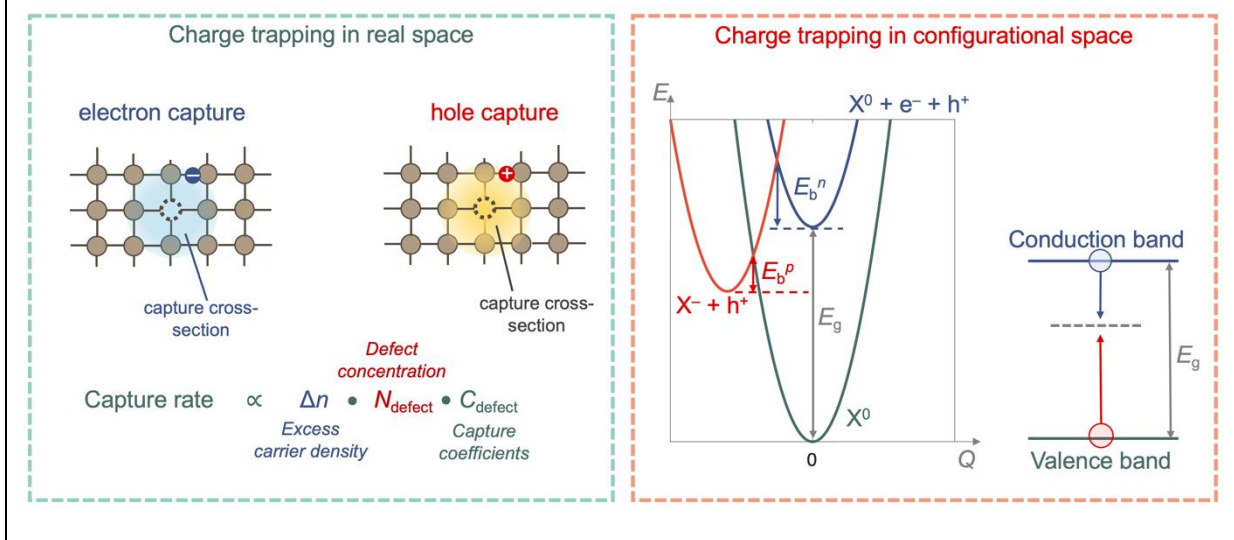
tolerance and the development of design rules that enable the discovery of defect tolerant semiconductors.

Box 1 | Charge-carrier trapping at defect sites

Point defects can create localized energy levels in crystalline materials. If these occur within the bandgap of a semiconductor, the associated charge transition levels (called traps) can capture electrons and/or holes, resulting in charge-carrier annihilation without emitting photons (*i.e.*, non-radiative recombination). Photoexcitation leads to the introduction of an excess carrier density with electrons (e^-) in the conduction band (CB) and holes (h^+) in the valence band (VB). The rate of charge trapping by defects will depend on this excess carrier density (Δn), along with both the concentration of active defects (N_{defect}) and their capture coefficients (C_{defect}), as shown in the left diagram below.

The microscopic process that determines C_{defect} can be visualized with a configuration coordinate diagram (sketched below, right panel), where each curve represents the energy of the system (E) as atoms are distorted from their equilibrium configuration (Q)^{39,40}. Starting with a neutral defect (X^0) in the presence of excess charge-carriers following photoexcitation (blue curve), by overcoming or tunnelling through the energy barrier E_b^n , an electron is captured, leading to a change in the defect charge state and distortion of the local structure (change in Q). The system becomes a negatively-charged defect with excess h^+ (red curve). Further overcoming energy barrier E_b^p leads to h^+ being captured by X^- , and the system re-entering into the ground state (green curve). During this cycle, the energy of an electron and hole (*i.e.*, the bandgap E_g) has been converted into heat through multi-phonon emission.

The overall non-radiative recombination rate depends on the carrier with the lowest capture rate, as described by the Shockley-Read-Hall model⁴¹. It is possible to obtain a low rate despite a high defect density by having traps close to one of the band-edges, such that the capture rate of one charge-carrier is minimized (Fig. 1c). These are called shallow traps, and are one route to defect tolerance. While standard analysis for conventional semiconductors typically considers the regime of weak distortion (small changes in Q) and harmonic potential energy surfaces (*i.e.*, parabolic E - Q curves), many defect charge transitions result in significant rearrangements in bonding (*e.g.*, dimer formation), especially for materials with soft structures. In this case, the energy gap between the trap level and band extrema is a poor proxy for charge-carrier capture, requiring consideration of the full potential energy surface⁴².



Defect tolerance in halide perovskites

Defining defect tolerance

A specific, widely-accepted definition of defect tolerance is currently elusive, partly because of continued debate over how defect tolerance arises, and partly because of the different probes used for evaluating the role of defects, from computational methods (Box 2) to experimental techniques, and with sensitivities ranging from the parts per trillion up to the percent level (Box

3). Adding to these difficulties, not all defects detected from measurements are recombination active. Analyzing defect concentrations alone without understanding what these species are makes it challenging to relate to non-radiative recombination rates.

Zakutayev *et al.* defined defect tolerance as “the tendency of a semiconductor to keep its properties despite the presence of crystallographic defects”³³. Brandt *et al.* subsequently built upon this to specify that materials could be defect tolerant if they 1) form low defect concentrations despite being processed rapidly at low-temperature, or 2) have minimal reductions in charge-carrier mobility and minority carrier lifetime despite the presence of “extrinsic, intrinsic, or structural defects”³². The latter definition was to recognize the importance of long minority-carrier diffusion lengths to achieve efficient performance, and that charge-carrier transport has historically limited the development of emerging thin film solar absorbers⁴³. It remains difficult to quantify “minimal reductions”, but for the purposes of materials screening, Buonassisi and co-workers proposed to use 1 ns minority-carrier lifetime as a critical threshold, since established thin-film solar absorbers needed lifetimes exceeding this to eventually reach 10% PCE in PVs⁴⁴. However, recent work has shown that overly relying on minority-carrier lifetime can be deceptive if self-trapped excitons or small polarons form, which can lead to prolonged decays in the measured photoexcited charge-carrier population, but give substantial reductions in mobilities, thus overall leading to short diffusion lengths^{45,46,47}. We therefore propose to refine this definition to “the effect, where a semiconductor, which readily forms free carriers, does not experience a substantial increase in its non-radiative recombination rate or reduction in charge-carrier mobilities when defects are present in high concentrations”, since materials with carrier localization, or which cannot readily separate excitons into free carriers, are inherently limited in performance.

Classifying the role of defects

A wide range of defect types exist in materials. These can be classified based on their scale and dimensionality. At the atomic scale, there are 0D point defects, comprised of one atom missing or misplaced (*e.g.*, vacancy, anti-site or interstitial). There are also structural defects, including 1D dislocations, 2D stacking faults and grain boundaries, and 3D twin domains, along with macroscopic voids, and defects occurring at surfaces and interfaces. Structural defects could be minimized through careful materials processing (*e.g.*, by increasing grain size or passivating surfaces), but 0D point defects are thermodynamically unavoidable, and are also the most straightforward to model (Box 2). The discussion of defect tolerance has therefore focussed on the effects of intrinsic point defects, and materials which tolerate point defects could also be more resilient to non-radiative recombination at structural defects.

The presence of a defect does not necessarily lead to an increase in non-radiative recombination. Defects must capture both an electron and hole to annihilate them. The role of defects in optoelectronic materials therefore strongly depends on the capture rates for charge-carriers, and this depends on the trap level and capture cross-section (Box 1), which describes the area around a defect where charge-carriers can be captured, typically in the range of 10^{-4} – 10^4 \AA^2 ^{48,49}. Defects that do not introduce a trap level in the bandgap are recombination-inactive, and are therefore classified as benign defects (*e.g.*, V_1^+ in $\text{CH}_3\text{NH}_3\text{PbI}_3$)⁵⁰. Such defects can give rise to defect tolerance; although, they may be active in other ways such as ion diffusion or chemical degradation. Similarly, defects with trap levels close to one of the band-edges and low capture-cross-sections are not recombination-active (Box 1), but will act as electron- (close to CBM) or hole-traps (close to VBM), with very low capture rates for the other charge-carrier. Recombination-active defects (termed recombination centres) tend to be

defects with trap levels close to mid-gap, with similar capture coefficients for both charge-carriers, especially if the capture coefficients are high. Such ‘killer defects’, which can be detrimental even in low concentrations, include V_{Se} in Sb_2Se_3 ⁵¹ and V_{S} in $\text{Cu}_2\text{ZnSnS}_4$ ⁵².

Furthermore, defects can exist in multiple charge states, especially if the species involved have higher valence (*e.g.*, V_{Bi} has more possible charge states than V_{Ag}), giving rise to multiple transition levels (Box 2). For example, while the (+/0) transition of V_{Se} in Sb_2Se_3 is inactive (slow carrier capture), the (2+/+) transition is fast, thus rendering V_{Se} a fast recombination centre⁵¹. Limitations of a single-trap model have been frequently observed, with the need to consider metastable charges or structural configurations that can also participate in the charge-trapping processes by introducing intermediate states^{48,53,54}.

Box 2 | Predicting the role of point defects

Defect behaviour can be modelled at the atomic scale. The addition, removal or rearrangement of atoms in a crystal can be described using quantum mechanical methods (*e.g.*, Density Functional Theory, DFT) or force fields (*e.g.*, classical or machine learning interatomic potentials). The key thermodynamic quantity that influences many derived properties is the defect formation energy (ΔH_f).

The advantage of quantum mechanical methods is that the electronic structure is rigorously described and there is no *a priori* assumption on the type of bonding that occurs in the material or at the defect site. The main disadvantage is the high computational cost. Defect properties are also sensitive to choices in the level of theory, with a high level (*i.e.*, a hybrid

exchange-correlation functional with relativistic effects) often required for accurate predictions of charge trapping with localized defect wavefunctions^{28,39,55–58}.

The first step of defect calculations consists of creating an atomic model for each native defect (*e.g.*, by removing a Bi^{3+} ion to model V_{Bi}^{3-} in Bi_2S_3). Since defects can capture charge-carriers from the host, thus undergoing structural rearrangements (see Box 1), a separate atomic model is needed for each charge state. Here it is key that each atomic model represents the most stable defect geometry for each charge state to obtain accurate predictions^{53,59,60}. The next step involves calculating the formation energy of each defect, which describes how easily they can form. These energies can be combined to predict the equilibrium concentrations and thus the dominant defect^{61,62}. There is progress in automating many of these steps in software packages^{63–68} such as *doped*⁶⁹ and *pydefect*⁷⁰.

The charge transition levels, which correspond to states that defects introduce within the bandgap, can also be analyzed and are typically classified as resonant, shallow or deep. Generally, defects that introduce deep levels are considered to be potential recombination centres. However, the position of the defect levels is not a reliable proxy for recombination activity (Box 1)^{39,52,71,72}. Instead, the non-radiative recombination rate for each defect can be calculated using the capture coefficients for electrons and holes (modelling the process depicted in Box 1)^{39,49,73,74} with packages like *CarrierCapture*⁷⁵ and *NonRad*⁷⁶. By considering the recombination rates for all detrimental defects, the overall effect on photovoltaic efficiency can be predicted⁴⁰.

Equilibrium growth conditions are commonly assumed, which can be used as an avenue to tune the defect populations (*e.g.*, growth temperature, ratio of the precursor elements or

partial pressure). By predicting defect concentrations for varying synthesis conditions, one can identify the conditions minimizing the density of harmful defects^{6,37}. Another factor that can affect the concentration of efficiency-killing defects is the incorporation of extrinsic dopants. For instance, impurities can reduce the concentration of detrimental defects by passivating them⁷⁷ (e.g., by binding to the native defect to form a benign complex^{30,78}, like filling a vacancy site^{51,79}). Alternatively, dopants can also act indirectly by modifying the density of free carriers (*i.e.*, the Fermi level), thus changing the concentration of the native defects⁶ and their effect on non-radiative recombination^{72,80}.

Models for defect tolerance

Several models have been proposed in the literature to explain one or more aspects of the observed defect tolerance of metal-halide perovskites.

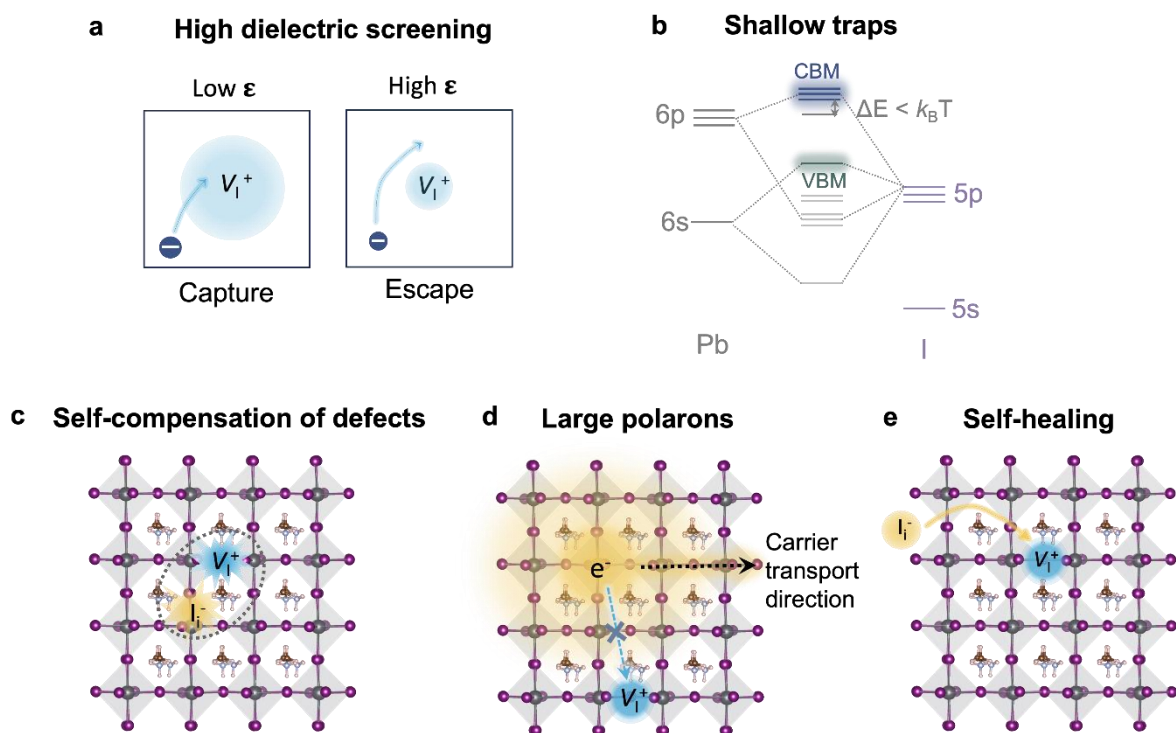


Fig. 2 | Models for defect tolerance in lead-halide perovskites. **a**, High dielectric screening, where the high dielectric constants reduce the interaction between free charge-carriers and

charged defects, thereby reducing the rate of carrier capture. **b**, Shallow trap model, where most traps are close to band-edges (within a few $k_B T$), and therefore benign. **c**, Self-compensation of defects, where defects form in charge-neutral combinations (*e.g.*, V_I^+ and I_I^-). **d**, Large polaron and low phonon energy model, where large polarons reduce the scattering and capture of charge-carriers by charged traps, and the low phonon energy leads to trapping being more difficult, with reduced nonadiabatic coupling constants. **e**, Self-healing, where fast ion migration promotes the annihilation of defects formed during exposure to damaging conditions.

High dielectric screening. The strength of the electrostatic interactions between charges in a crystal depends on the dielectric constant. This constant influences relevant processes, ranging from the binding energy between electrons and holes to form excitons, the scattering between charge-carriers and charged defects that may limit mobility, and the rates at which defects capture and annihilate charge-carriers. In standard inorganic semiconductors, the static dielectric constant is comprised of two components: a high-frequency optical response (ϵ_{optic}), and a low-frequency ionic response from phonons (ϵ_{ion}). For $\text{CH}_3\text{NH}_3\text{PbI}_3$, the reported values of ϵ_{optic} (4–7) are typical for photovoltaic absorbers, while ϵ_{ion} is substantially larger (17–29) due to the low-frequency infra-red active phonon modes. However, there is an additional component for the reorientation of the polar CH_3NH_3^+ molecule, which has been measured as between 13–37 depending on the temperature and frequency range⁸¹. Together the dielectric screening far exceeds the static dielectric constants of Si (12) or CdTe (10). These observations motivated the search for other highly polarizable semiconducting materials³².

Shallow trap model. In 2014, Yin *et al.* reported defect calculations for $\text{CH}_3\text{NH}_3\text{PbI}_3$ that concluded: “dominant intrinsic defects create only shallow levels, which partially explain the long electron-hole diffusion length and high open-circuit voltage”³¹. The finding that the dominant point defects in halide perovskites do not introduce deep levels has held up well in subsequent studies^{82,83}. This observation does not mean that deep states cannot form, for

example, there is a significant body of literature on deep traps introduced by halide interstitials or lead antisites⁷¹, but fortunately, they do not support rapid non-radiative recombination cycles^{84,85}.

Microscopically, the tendency to form shallow traps was attributed to the anti-bonding nature of the upper valence band (Pb 6s – I 5p) and lower conduction band (Pb 6p – I 5p), as illustrated in Fig. 2b. In this orbital arrangement, the atomic orbitals from which *non-bonding* defect states arise are located close to the band edges, and thus often lead to shallow or resonant states^{6,86}. However, deep states can still form when there is significant hybridization between the defect dangling bonds, since the resulting (anti)bonding state will have (higher) lower energy than the original atomic orbitals⁸⁷. Such behaviour is exemplified by the halide vacancy in the CsPbX₃ family, whose (+/0) donor level changes from shallow to deep through the halide series (I, Br, Cl)⁸⁸ due to the decreased lattice constant (thus smaller Pb–Pb distance in CsPbCl₃) and increased ionicity which favour the hybridization of Pb orbitals.^{89,90} The relationship between increased lattice constant and reduced trap-mediated recombination has been further confirmed from carrier capture calculations of I_i in orthorhombic FAPI, where a 1% lattice expansion reduces the carrier capture coefficient by one order of magnitude⁹¹.

Low density of deep defects. An argument put forward against the shallow defect model is that some low-energy defects (*e.g.*, V_H and I_i in MAPI)^{92,93} may act as rapid non-radiative recombination centres. However, these studies seem to be limited by either modelling less common defect species (*i.e.*, V_H corresponds to forming methylamine, CH₃NH₂, which forms a gas that would evaporate under typical synthesis and processing conditions) or disagreements with other theoretical studies that also investigated carrier capture by I_i⁸⁴. More importantly,

they would challenge the experimentally observed long charge-carrier lifetimes found in LHPs. These discrepancies between theoretical studies illustrate the challenges for accurately modelling defects in LHPs due to the instability of the cubic phase at 0 K, and the soft potential energy surface that supports significant thermal motion, including dynamic octahedral tilting around room temperature.

Self-compensation of defects. Most LHPs are intrinsic semiconductors, with low charge-carrier concentrations in the dark⁹⁴, and are resistant to extrinsic *n*- or *p*-type doping. Sn-based compounds are an exception, due to the oxidation of Sn(II) to Sn(IV)⁹⁵. One model used to explain the intrinsic behaviour is self-compensation. Rather than forming charged defects that are compensated by electrons or holes, the defects form in predominately charge-neutral combinations. Compensation can occur in the form of Schottky (vacancy) disorder, *i.e.*, $[V_A^-] + [V_B^{2-}] = 3[V_X^+]$, or Frenkel (vacancy/interstitial) disorder, *i.e.*, $[V_X^+] = [X_i^-]$ ⁹⁶. The thermodynamic cost to form ensembles of compensated defects is low⁹⁶. This introduces an insensitivity to the growth conditions and large defect concentrations can be supported without the detrimental effects of high carrier concentrations that would otherwise limit solar cell efficiency. This model has been further validated by posterior theoretical studies on MAPI, which predicted that the vacancies V_I^+ , V_{Pb}^{2-} and V_{MA}^- form in high concentrations and follow a ratio ranging between 9.1:3.5:2 and 9.5:2.3:3.8 from MAI rich to PbI_2 rich conditions, respectively, thus in agreement with the formation of a stoichiometric amount of cation and anion vacancies⁹⁷. In addition, the predicted high vacancy concentration supports the observed high ionic conductivities since they facilitate mass transport.

Polaronic model. Zhu and co-workers proposed that the defect tolerance of LHPs occurs due to the formation of large polarons^{98–100}. Large polarons arise due to the weak to intermediate coupling between charge-carriers and longitudinal optical (LO) phonons, and there is now a plethora of evidence for large polaron formation from temperature-dependent mobility, optical pump terahertz probe spectroscopy (OPTP) and transient absorption spectroscopy and transient electron diffraction measurements, among others^{47,98}. By forming large polarons, the long-range Coulombic potential experienced by charge-carriers from charged defects is weakened. Large polarons also have higher effective masses than free carriers, with the larger momentum reducing scattering by defect-induced phonons. Additionally, the shielding effect may add an extra energy barrier to the recombination of two large polarons with opposite charges, which slows the recombination process and increases the charge-carrier lifetime^{1,8,9}. On the other hand, a disadvantage of forming large polarons is the reduction in charge-carrier mobility. Fortunately, the low deformation potential in electronically 3D halide perovskites ensures that small polarons do not form, such that charge-carriers remain delocalized, and mobilities $> 50\text{--}200 \text{ cm}^2 \text{ V}^{-1} \text{ s}^{-1}$ are achievable¹⁰¹, which is important for realizing $>1 \text{ }\mu\text{m}$ diffusion lengths in polycrystalline thin films¹⁰².

Low-energy phonons. A key feature of LHPs is the soft nature of their structure formed of flexible corner-sharing octahedra, with bulk moduli an order of magnitude smaller than metal oxides^{103,104} (*e.g.*, $20\pm 2 \text{ GPa}$ for MAPbI_3 ¹⁰⁵ vs. 390 GPa for $\alpha\text{-Al}_2\text{O}_3$ ¹⁰⁶). The underlying vibrational spectrum is complex, ranging from low-frequency modes ($<100 \text{ cm}^{-1}$) associated with octahedral tilting and deformations to high-frequency modes ($>100 \text{ cm}^{-1}$) linked to molecular vibrations¹⁰⁷. The low-frequency infra-red active phonon modes make the largest contribution to electron-phonon coupling and result in an upper limit to the charge-carrier mobility¹⁰⁸. Kirchartz *et al.* pointed out that within the Shockley-Read-Hall model of non-

radiative recombination, a low phonon energy is beneficial. As carrier trapping is a multi-phonon emission process, a larger number of phonons need to be emitted if the phonon energy is smaller, making carrier trapping less likely to occur¹⁰⁹. The role of phonon modes has also been explored using non-adiabatic molecular dynamics (NAMD) simulations that track the non-adiabatic coupling constant (NAC) between electrons/holes with defect states at finite temperatures. Low NAC values have been linked to defect tolerance including contributions from differences in wavefunction overlap, as well as contributions from the nuclear velocity of the heavy Pb and I atoms^{103,104}. While NAMD is useful to model the dynamics of defects in excited states, it is important to consider all recombination mechanisms with appropriate charge-carrier and defect densities to estimate the contribution of changes in NAC to device performance. These factors can increase the predicted carrier lifetimes from ns to ms¹¹⁰.

Self-healing. Self-healing refers to the ability of a material to autonomously recover its original performance after being damaged by an external stressor. It has been proposed to explain the high radiation resistance of LHPs^{111–113}, and their performance recovery during light-dark cycles^{114–117}. Microscopically, self-healing has been attributed to rapid ion migration^{26,111,114,118}. External perturbations, like high-energy radiation¹¹¹, light-illumination¹¹⁴, stress¹¹⁹, crystal cleavage¹²⁰, or chemical agents, can create defects. After the perturbation ceases, ions can migrate and return to their energetically favoured lattice positions, thus annihilating the defects¹²¹. Beyond defect migration, self-healing has also been linked to the low dissociation energy of LHPs into their binary constituents¹²², which enables the rapid reformation of the LHP after damage. For example, the self-healing behaviour induced by chemical agents was investigated by Zhou and coworkers, who demonstrated that a mild stimulus (methylamine gas) can induce the formation of an intermediate liquid phase (*e.g.*, dissociation), which transforms into a smooth “defect-free” film after removing the gas¹²³.

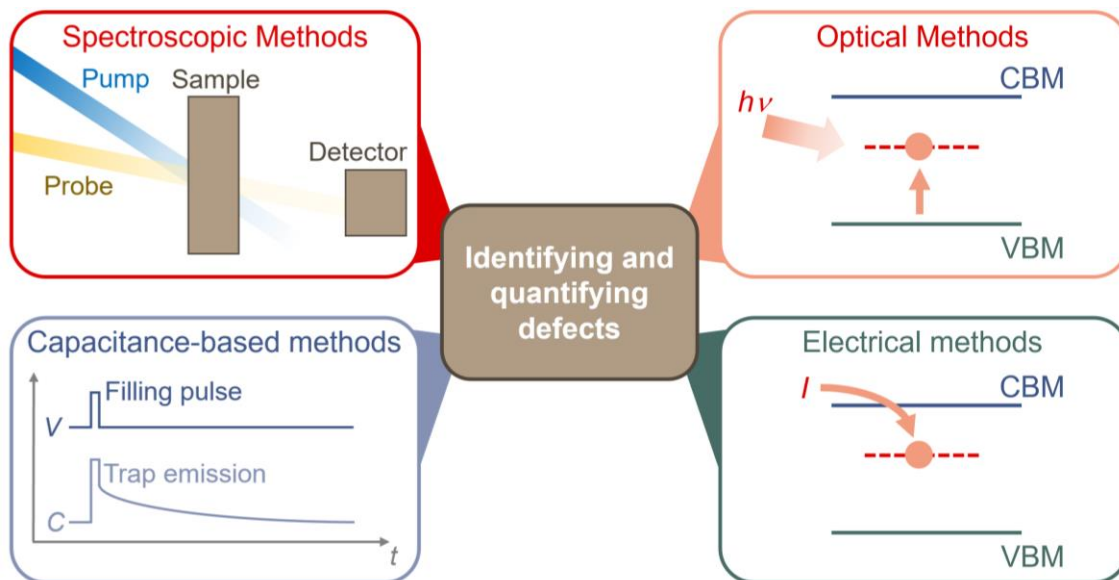
Box 3 | Measuring the point defects present and their effects

The density, energy and capture cross-sections of defects, along with their effects on non-radiative recombination, can be determined using a wide range of spectroscopic, optical, electrical and capacitance techniques. Owing to the multi-varied nature of how each technique works, we focus on the overarching principles, the strengths, and challenges of using each method on the materials considered in this review.

Spectroscopic methods indirectly measure the effects of defects on non-radiative recombination, and have the advantages of being non-destructive and not requiring pinhole-free films. Common techniques include steady-state photoluminescence (PL) quantum yield (measuring the fraction of recombination events that are radiative)¹²⁴, and time-resolved techniques, such as time-resolved PL¹²⁵ and transient absorption spectroscopy¹²⁶. With these methods, the sample is optically pumped, but other pump sources can be used, *e.g.*, electrons in cathodoluminescence spectroscopy¹²⁷, and positrons in positron annihilation spectroscopy³⁸. Often these techniques are used together, but extracting recombination rate constants requires the development of a model to fit the time-resolved data^{44,128}, which is typically a simplification of the many complex processes occurring.

Relative changes in defect concentrations can be determined by measuring energetic transitions below the bandgap. However, the increase in sub-gap absorption due to defects is typically orders of magnitude below band-edge absorption. Techniques sensitive to these small changes include photothermal deflection spectroscopy¹²⁹, surface photovoltage measurements¹³⁰, and Fourier transform photocurrent spectroscopy¹³¹. However, these techniques are unable to directly quantify defect densities or identify the defects present, and are more useful for qualitative comparisons between samples.

Quantification of defect concentrations can be achieved through space-charge limited current density measurements¹³². This method requires a single-carrier device to be made, and the voltage swept until traps are filled. The trap density can be determined from the voltage at which trap filling occurs, but this assumes an ideal device, which often does not occur. More accurate ways to quantify defect density, as well as capture cross-sections, involve monitoring changes in the capacitance of a device due to trap filling/de-trapping. Prominent techniques include deep-level transient spectroscopy (DLTS)¹³³ and admittance spectroscopy¹³⁴. For example, DLTS is sensitive to defects at the parts per trillion level¹³⁵. However, these techniques cannot directly identify the defects giving rise to traps, require the fabrication of devices (*i.e.*, requires compact films), and are unable to detect shallow defects^{133,134}. Ion migration will affect the capacitance profiles, requiring consideration of how these affect the measurements³⁵. Furthermore, DLTS/admittance spectroscopy may present lower estimates of trap densities, and need to be treated with caution.



Challenges in generalizing defect tolerance

A core motivation for unravelling the origins of defect tolerance in LHPs is to replicate this feature in broader classes of semiconductors, particularly nontoxic and stable compounds. Semiconductors developed on this basis are termed ‘perovskite-inspired’, and have especially focussed on materials with heavy main group cations that have stable valence ns^2 electron pairs (In^+ , Sn^{2+} , Sb^{3+} , Bi^{3+}). In this section, we cover key points in the progress of these materials in PVs, before discussing the challenges in obtaining defect tolerance in chemistries beyond halide perovskites.

Progress of Perovskite-Inspired Materials (PIMs) in Photovoltaics

To give a sense for the progress in this area, we cover key perovskite-inspired materials (PIMs), namely Sn and Ge perovskites, Bi-halide compounds, and antimony chalcogenides. These are most relevant for the discussion below. More detailed coverage of this broad materials space, including In-based compounds, can be found in Refs. 136–140. Whilst the exploration of some compounds predates the development of LHP PVs, it is useful to consider these as PIMs because they are electronically, structurally or chemically analogous to LHPs, and the motivation is the same – to develop an efficient, nontoxic and stable alternative to halide perovskite PVs.

Sn and Ge perovskites. The greatest success has been in materials most similar to LHPs, the isostructural tin-based perovskites (ASnI_3 , $\text{A} \in \{\text{MA}, \text{FA}, \text{Cs}\}$). FASnI_3 PVs have now reached PCEs of 15.7% (Fig. 3), with a PL lifetime of 207 ns. However, Sn perovskites have limited stability, due to the facile oxidation of Sn(II) to Sn(IV), forming reactive defects that accelerate

degradation. As such, excess SnX_2 halides and reducing additives, such as Sn powder or hydrazine vapour, and its derivatives are widely used in high-efficiency Sn perovskite solar cells¹⁴¹. Careful encapsulation of Sn perovskite devices, or the formation of protective layers (e.g., SnCl_2 covering grains) are essential¹⁴². Similarly, Ge(II) is easily oxidized, leading to the formation of detrimental defects and competitive phases^{143,144}, and with few exceptions (e.g., CsGeI_3) have bandgaps exceeding 2 eV¹⁴⁵. There is therefore limited work on Ge-based perovskites.

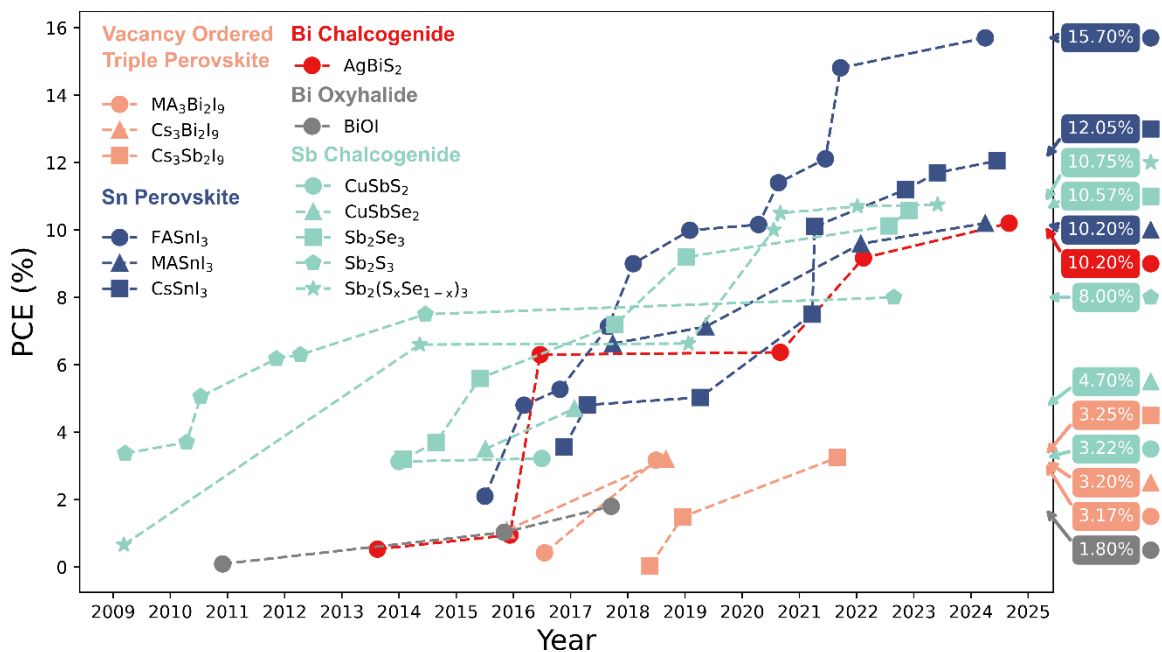


Fig 3 | Progress of perovskite-inspired materials as solar absorbers. Plot of the progress in the photovoltaic power conversion efficiency (PCE) over time of key compounds. References by material: $\text{MA}_3\text{Bi}_2\text{I}_9$ ^{146,147}, $\text{Cs}_3\text{Bi}_2\text{I}_9$ ^{148,149}, $\text{Cs}_3\text{Sb}_2\text{I}_9$ ^{150–152}, FASnI_3 ^{153–163}, MASnI_3 ^{164–167}, CsSnI_3 ^{168–175}, AgBiS_2 ^{176–181}, BiOI ^{182–184}, CuSbS_2 ^{185,186}, CuSbSe_2 ^{187,188}, Sb_2S_3 ^{189–195}, Sb_2Se_3 ^{196–201}, $\text{Sb}_2(\text{S}_x\text{Se}_{1-x})_3$ ^{202–208}. Refer to Supplementary Table 1 for details.

Bi-halide materials. While Bi-based materials have been the subject of much research due to their low toxicity²⁰⁹, a common characteristic is self-trapping, which substantially limits mobilities and diffusion lengths, gives rise to larger open-circuit voltage losses, and can lead to unavoidable energy loss channels (see carrier-phonon coupling section for further

discussion). As such, there is poor performance among many Bi-based materials, *e.g.* MA₃Bi₂I₉¹⁴⁷, NaBiS₂²¹⁰, and BiI₃²¹¹, all of which form small polarons or self-trapped excitons. However, recent work has shown self-trapping is not universal among Bi-based materials, and both BiOI and homogeneously-disordered AgBiS₂ have mobilities significantly above unity^{212,213}. There is therefore hope that Bi-based PIMs could be developed into efficient devices, and indeed AgBiS₂ has already reached a certified PCE of 8.85%¹⁷⁷, with lab-measured PCEs now exceeding 10% (Fig. 3)¹⁸¹.

Antimony chalcogenides. The isostructural antimony chalcogenides, Sb₂Se₃, Sb₂S₃ and Sb₂(Se,S)₃, are promising systems, with highest reported efficiencies of 10.57%²¹⁴, 8.00%¹⁸⁹ and 10.75%²⁰⁸, respectively, but are limited by low V_{OC} . Of the binary compounds, the selenide analogue shows the best efficiencies, where process control of the defects present is key to high-efficiency devices. There has been some debate over whether the critical performance losses originate from deep defects or self-trapping (see carrier-phonon coupling section). Nevertheless, reducing the grain boundary density, and passivating interfaces (*e.g.*, through the use of chelating or lanthanide additives) has been beneficial for improving V_{OC} and device performance^{215,216}.

Ternary cuprous compounds include CuSbSe₂ and CuSbS₂, both of which showed early promise in their performance, but have since stagnated (with peak PCEs of 4.7%¹⁸⁶ for CuSbSe₂ and 3.2%¹⁸⁷ for CuSbS₂; Fig. 3). These isostructural materials have been predicted to be defect tolerant²¹⁷. For both materials, a Cu-poor growth condition is preferred, as the dominant V_{Cu} results in p-type character *via* self-compensation. Poor performance has been attributed to low J_{sc} values, yet the reasons remain unexplored²¹⁸. Morphological defects, such

as voids and delamination, are also common and device-limiting. Additionally, it has been proposed that grain boundary defects may be strongly detrimental in this class, as with CdTe^{24,14}.

Challenges in Achieving Defect Tolerance in Perovskite-Inspired Materials

Diversity of the electronic structure. Early efforts to discover PIMs were driven by the dielectric screening and shallow trap models (Fig. 2a,b)^{32,44}. However, these models have not been able to pinpoint the discovery of defect tolerant semiconductors. For example, Zakutayev *et al.* proposed an electronic structure model for defect tolerance in Cu₃N resembling the model for LHPs. In Cu₃N, cation-anion orbital interactions produce a pair of bonding-antibonding states in both the upper valence and lower conduction bands (Fig. 4a)³³. Although this was proposed to increase the likelihood of forming shallow defects³³, recent work has suggested Cu_i as a potential deep trap²¹⁹. LHPs similarly form a bonding-antibonding pair within the upper VB, although the CBM has an antibonding state (Fig. 2b). Such an electronic structure improves the likelihood of shallow acceptor defects. Buonassisi and co-workers therefore proposed to search for PIMs where the upper valence band has a significant contribution from the cation valence s² electrons, as they could result in similar bonding-antibonding states as in LHPs^{32,44}.

However, this qualitative model does not account for the degree of interaction between cation/anion orbitals or the specific crystal environments. In particular, Bi has a higher effective nuclear charge than Pb, and this results in the 6s² orbital being deeper and more misaligned with the anion orbitals, resulting in a less disperse VB (higher effective mass), along with an increased tendency to form deeper traps.

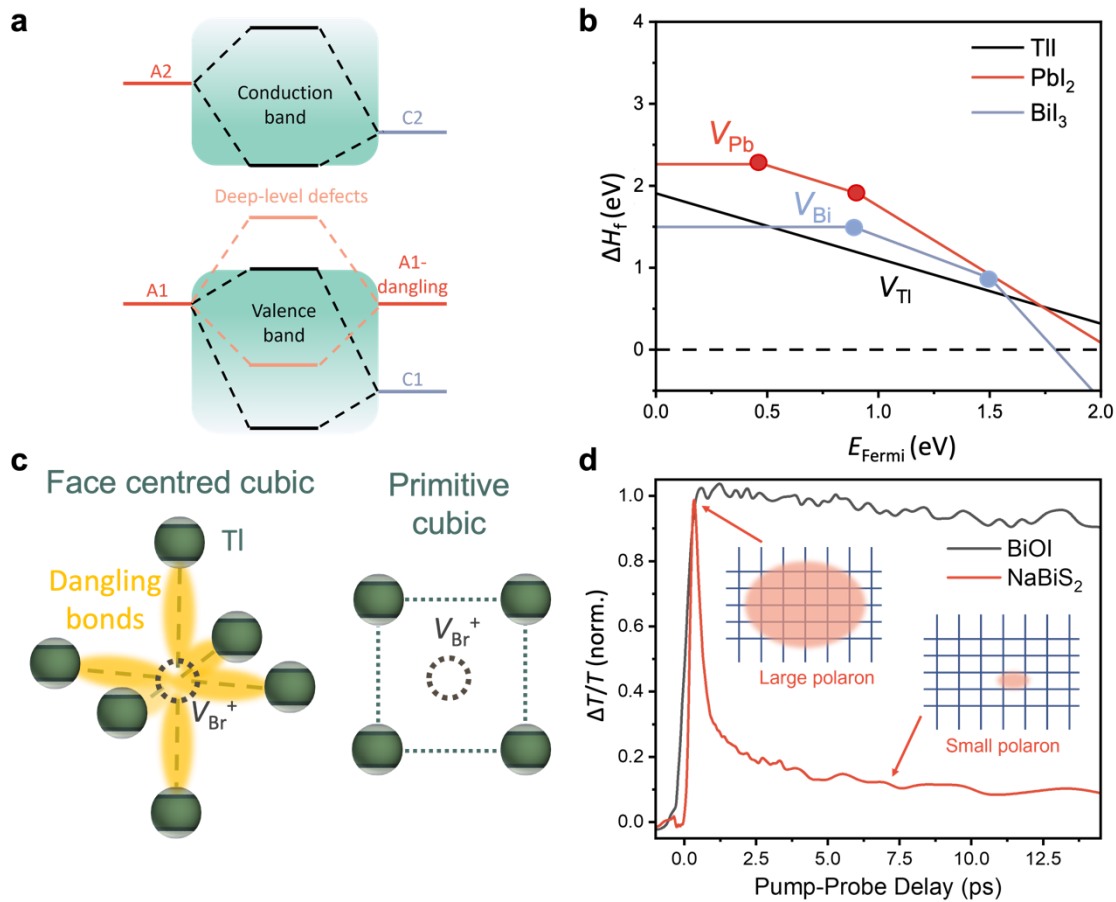


Fig 4 | Performance bottlenecks in emerging perovskite-inspired materials. **a**, Energy misalignment leading to the presence of deep defects. A, A-dangling, and C refer to the anion, anion dangling bond, and cation orbitals, respectively. **b**, Calculated formation energies ΔH_f of the cation vacancies in TlI, PbI_2 , and BiI_3 ²²⁰. **c**, Strong overlap of dangling bonds due to V_{Br^+} in a face centred cubic lattice of TlBr (left), vs. weak dangling bond overlap in the primitive cubic polymorph (right). **d**, Normalized photoconductivity kinetics of BiOI and NaBiS_2 ^{210,213}. In NaBiS_2 , delocalized large polarons initially occur after photoexcitation, but due to strong electron-phonon coupling, small polarons rapidly form on a ps timescale, leading to localized small polarons and a sharp decrease in photoconductivity. By contrast, the photoconductivity of BiOI slowly decays because carrier localization does not occur.

Strength of interaction between dangling bonds. When defects form, dangling bonds can hybridize, forming bonding-antibonding states. The (anti)bonding states can occur within the bandgap, becoming recombination-active traps (Fig. 4a). Stronger hybridization leads to greater bonding-antibonding state splitting, increasing the likelihood of deep traps. This

hybridization strength between dangling bonds depends on their spatial and energetic separation. Therefore, traps become deeper when the lattice parameter decreases (see shallow trap model sub-section), or when the cation-anion orbitals are more poorly aligned (*i.e.*, as C1 is further from A1 in Fig. 4a). For example, in comparing iodides of heavy main group cations with stable $6s^2$ electron pairs (Tl to Bi), the cation vacancy forms a deeper level going across this series (Fig. 4b) due to the increasing energetic separation between cation-anion orbitals (C1-A1 in Fig. 4a). Furthermore, the higher cation oxidation state leads to a larger number of transition levels (Fig. 4b), thus increasing the likelihood of deep traps²²⁰. The role of spatial separation can be illustrated by BiOI, where the long Bi-I bonds (3.4 Å) weaken the interaction between Bi dangling orbitals, thus forming a shallow V_I , in contrast with the deeper V_O and the shorter Bi-O bonds (2.3 Å)^{184,221}.

The strength of interaction between dangling bonds is also affected by the ionic radius and anion coordination number. For instance, large anions coordinated with small cations, as well as low anion coordination numbers, have larger inter-cation separation, which could result in shallow anion vacancies²²⁰.

The discussion thus far has been on compounds where the cation/anion orbitals hybridize. Another way to form shallow traps involves materials with little interaction between the cation and anion orbitals, such that forming vacancies would not lead to dangling bonds. This could be obtained either by forming a structure with separate cation/anion sub-lattices (*e.g.*, TlBr in the primitive cubic rather than face centred cubic lattice; Fig. 4c)²²², or by having cation/anion orbitals with sufficient energetic separation to avoid mixing (*e.g.*, monolayer transition metal dichalcogenides)²²³.

Low dimensionality. A critical difference between most of the PIMs explored and LHPs is the lower structural and electronic dimensionality of PIMs, leading to important challenges. Firstly, excitons can form more easily, impeding charge-carrier extraction. Secondly, lower dimensionality favours wider bandgaps, with values close to 2 eV²²⁴ for most PIMs vs. 1.5–1.6 eV for MAPbI₃^{225,226}. A wider bandgap reduces the optical dielectric constant since fewer free carriers are available for polarization, thus reducing the dielectric screening of charged defects. Thirdly, in some cases, low dimensionality could facilitate defect formation. For example, although Sb₂Se₃ has been considered promising because it has achieved >10% PCE in PV devices (Fig. 3), both DFT calculations and DLTS measurements indicate its lack of defect tolerance^{51,227,228}. This has been attributed to the quasi-1D crystal structure of Sb₂Se₃, where the [Sb₄Se₆]_n chains are bound through *van der Waals* interactions. These weak interactions, in addition to the valence alternation of Sb and Se²²⁹, allow significant structural reconstructions upon defect formation, thus stabilizing many charge states and leading to many defect levels. Finally, low electronic dimensionality also increases the likelihood of carrier localization, as will be discussed next.

Carrier-phonon coupling. Charge-carriers can couple with lattice vibrations, giving rise to quasi-particles known as polarons²³⁰. Strong electron-phonon coupling can localize the carrier wavefunction within a unit cell, which is known as carrier localization or self-trapping. This substantially reduces mobilities (typically to <1–10 cm² V⁻¹ s⁻¹), limiting diffusion lengths, and is unavoidable even in defect-free materials. The past decade of work has revealed the significant presence of self-trapping in PIMs, especially Bi-based materials^{46,231,232}, including BiI₃²³³, NaBiS₂²¹⁰, Cu-Ag-Bi-I compounds^{211,234}, Cs₂AgBiBr₆²³¹, and other silver-bismuth

elpasolites. This originates from their low electronic dimensionality, which can lead to barrierless carrier localization, especially when there is strong carrier-acoustic phonon coupling. Such a process can be observed experimentally by monitoring the photoconductivity, where the signal significantly decreases within a ps, as demonstrated in the case of NaBiS₂ (Fig. 4d).

Carrier localization can change the optoelectronic behaviour of materials, such that deep trap states no longer play a dominant role. For example, introducing defects at the percentage level in NaBiS₂ barely changed the decay of the excited state, which proceeded on the microsecond timescale²¹⁰. This is due to the formation of small electron and hole polarons, spatially separated on Bi and S sites, respectively, which lowers the likelihood of both charge-carriers annihilating *via* the same defect. Whilst this gives the appearance of defect tolerance, strong localization leads to low charge-carrier mobilities ($<0.1 \text{ cm}^2 \text{ V}^{-1} \text{ s}^{-1}$; Fig. 4d), thus limiting diffusion lengths and charge-carrier extraction. Developing efficient PIMs therefore necessitates compounds with free charge-carriers. By studying CuSbSe₂, we rationalized that this may be found in compounds with a layered structure. This results in a lower deformation potential, because the strains to the unit cell from a propagating acoustic wave are mostly relaxed through changes in inter-layer gaps, rather than bond lengths. Furthermore, orbital hybridization across inter-layer gaps results in a higher electronic dimensionality (*e.g.*, CuSbSe₂ has a nearly 3D lower CB), reducing the likelihood of carrier localization being energetically favourable.

Finally, electron-phonon coupling can also create a non-radiative loss channel that does not arise from defects. We found this in BiOI, where the coupling between charge-carriers and

interlayer breathing modes significantly distorts the potential energy surface, such that the ground and excited states approach each other, and excitations can then directly return to the ground state following a non-radiative pathway.

Conclusions and outlook

Defect tolerance is key to developing high-performance and cost-effective optoelectronic materials. The exceptional performance of LHPs has revived this topic, which has been examined from a wide range of perspectives. Although this has led to different interpretations, at its core, we believe defect tolerance to mean that the semiconductor maintains free charge-carriers, low non-radiative recombination rates, and high mobilities despite the introduction of defects, which then affords it with the long charge-carrier transport lengths necessary to approach its optical limits in performance. A wide range of models have been proposed for defect tolerance in LHPs. The most popular are the shallow trapping and dielectric screening models, but they have yielded only few materials that may exhibit defect tolerance, and none that have yet matched the performance of LHP PVs. A key issue is that these models do not account for the strength of cation-anion orbital overlap, or the hybridization between dangling bonds. Detailed studies into binary halide PIMs have proven valuable in refining these design criteria. At the same time, there are still several outstanding questions that need to be addressed.

Firstly, the soft and dynamic nature of the LHP structure has complicated the interpretation of the role of traps via the Shockley-Read-Hall model, questioning whether the trap energy is a reasonable proxy for the carrier capture rate. In-depth investigations combining high-level theory with state-of-the-art characterization that can probe similar length- and time-scales will be necessary to resolve this debate.

Secondly, a greater mechanistic understanding of self-healing is required, which will establish the importance of ion transport both in the dark and under illumination. Currently, self-healing is poorly understood computationally due to the long timescales involved, but there is growing experimental evidence of its importance for the manifestation of defect tolerance in LHPs. If self-healing requires significant mass transport, this would open up important questions regarding whether there would be a compromise with the stability of devices under operation.

Thirdly, it will be critical to consider the role of carrier-phonon coupling. This includes understanding whether a trade-off is required between factors affecting both defect tolerance and carrier localization. For example, lower-energy phonon modes contribute to defect tolerance, but would increase the strength of Fröhlich coupling, reducing mobilities. Similarly, higher Born-effective charges increase the ionic contribution to the dielectric constant, which leads to improved screening of carriers from charged defects, but would also increase Fröhlich coupling. Beyond the current focus on band-edge charge-carriers, an important challenge will be to extend the understanding of defect tolerance to hot carriers. In particular, understanding how traps influence the hot carrier cooling process, hot phonon bottleneck effect, Auger reheating and the overlap of polarons will be critical to achieving hot carrier solar cells that can overcome the radiative limit.

Overall, addressing these challenges could improve our understanding of the multifaceted nature of defect tolerance, not only for the current focus on intrinsic defects, but also extended to extrinsic impurities²³⁵. Together, these can lead to new avenues to create efficient and cost-effective semiconductors.

References

1. Ballif, C., Haug, F.-J., Boccard, M., Verlinden, P. J. & Hahn, G. Status and perspectives of crystalline silicon photovoltaics in research and industry. *Nat. Rev. Mater.* **7**, 597–616 (2022).
2. Nayak, P. K., Mahesh, S., Snaith, H. J. & Cahen, D. Photovoltaic solar cell technologies: analysing the state of the art. *Nat. Rev. Mater.* **4**, 269–285 (2019).
3. Nishiyama, H. *et al.* Photocatalytic solar hydrogen production from water on a 100-m² scale. *Nature* **598**, 304–307 (2021).
4. Andrei, V. *et al.* Floating perovskite-BiVO₄ devices for scalable solar fuel production. *Nature* **608**, 518–522 (2022).
5. Holmes-Gentle, I., Tembhurne, S., Suter, C. & Haussener, S. Kilowatt-scale solar hydrogen production system using a concentrated integrated photoelectrochemical device. *Nat. Energy* **8**, 586–596 (2023).
6. Walsh, A. & Zunger, A. Instilling defect tolerance in new compounds. *Nat. Mater.* **16**, 964–967 (2017).
7. Zhou, Y., Poli, I., Meggiolaro, D., De Angelis, F. & Petrozza, A. Defect activity in metal halide perovskites with wide and narrow bandgap. *Nat. Rev. Mater.* **6**, 986–1002 (2021).
8. Zhou, J. *et al.* Highly efficient and stable perovskite solar cells via a multifunctional hole transporting material. *Joule* **8**, 1691–1706 (2024).
9. LONGi Green Energy Technology. LONGi Sets New World-Record for Silicon Solar Cell Efficiency, Launching 2nd Generation Ultra-Efficient BC-Based Module. <https://www.longi.com/en/news/longi-hi-mo9-bc-world-record/> (2024).
10. Liu, S. *et al.* Buried interface molecular hybrid for inverted perovskite solar cells. *Nature* 1–3 (2024) doi:10.1038/s41586-024-07723-3.

11. Dale, P. J. & Scarpulla, M. A. Efficiency versus effort: A better way to compare best photovoltaic research cell efficiencies? *Sol. Energy Mater. Sol. Cells* **251**, 112097 (2023).
12. NREL. Best Research-Cell Efficiency Chart. <https://www.nrel.gov/pv/cell-efficiency.html> (2024).
13. Tiedje, T., Yablonovitch, E., Cody, G. D. & Brooks, B. G. Limiting efficiency of silicon solar cells. *IEEE Trans. Electron Devices* **31**, 711–716 (1984).
14. Das, S. K. & Morris, G. C. Preparation and properties of CdS/CdTe thin film solar cell produced by periodic pulse electrodeposition technique. *Sol. Energy Mater. Sol. Cells* **30**, 107–118 (1993).
15. Akkerman, Q. A., Rainò, G., Kovalenko, M. V. & Manna, L. Genesis, challenges and opportunities for colloidal lead halide perovskite nanocrystals. *Nat. Mater.* **17**, 394–405 (2018).
16. Huang, H., Bodnarchuk, M. I., Kershaw, S. V., Kovalenko, M. V. & Rogach, A. L. Lead Halide Perovskite Nanocrystals in the Research Spotlight: Stability and Defect Tolerance. *ACS Energy Lett.* **2**, 2071–2083 (2017).
17. Xu, J. *et al.* Defect Tolerance of Mixed B-Site Organic–Inorganic Halide Perovskites. *ACS Energy Lett.* **6**, 4220–4227 (2021).
18. Ye, J. *et al.* Defect Passivation in Lead-Halide Perovskite Nanocrystals and Thin Films: Toward Efficient LEDs and Solar Cells. *Angew. Chem. Int. Ed.* **60**, 21636 (2021).
19. Shin, S. S. *et al.* Colloidally prepared La-doped BaSnO₃ electrodes for efficient, photostable perovskite solar cells. *Science* **356**, 167–171 (2017).
20. Polman, A., Knight, M., Garnett, E. C., Ehrler, B. & Sinke, W. C. Photovoltaic materials: Present efficiencies and future challenges. *Science* **352**, aad4424 (2016).
21. Lindmayer, J. & Allison, J. F. The violet cell: An improved silicon solar cell. *Sol. Cells* **29**, 151–166 (1990).

22. Green, M. A. The path to 25% silicon solar cell efficiency: History of silicon cell evolution. *Prog. Photovolt. Res. Appl.* **17**, 183–189 (2009).
23. Green, M. A. Silicon solar cells: evolution, high-efficiency design and efficiency enhancements. *Semicond. Sci. Technol.* **8**, 1 (1993).
24. Blakesley, J. C. *et al.* Roadmap on Photovoltaic Absorber Materials for Sustainable Energy Conversion. Preprint at <https://doi.org/10.48550/arXiv.2310.19430> (2023).
25. Park, J. *et al.* Controlled growth of perovskite layers with volatile alkylammonium chlorides. *Nature* **616**, 724–730 (2023).
26. Cahen, D., Kronik, L. & Hodes, G. Are Defects in Lead-Halide Perovskites Healed, Tolerated, or Both? *ACS Energy Lett.* **6**, 4108–4114 (2021).
27. Min, H. *et al.* Efficient, stable solar cells by using inherent bandgap of α -phase formamidinium lead iodide. **366**, 749–753 (2019).
28. Meggiolaro, D. *et al.* Iodine chemistry determines the defect tolerance of lead-halide perovskites. *Energy Environ. Sci.* **11**, 702–713 (2018).
29. Hangleiter, A. Nonradiative recombination via deep impurity levels in silicon: Experiment. *Phys. Rev. B* **35**, 9149–9161 (1987).
30. Zhang, S. B., Wei, S.-H. & Zunger, A. Stabilization of Ternary Compounds via Ordered Arrays of Defect Pairs. *Phys. Rev. Lett.* **78**, 4059–4062 (1997).
31. Yin, W.-J., Shi, T. & Yan, Y. Unusual defect physics in $\text{CH}_3\text{NH}_3\text{PbI}_3$ perovskite solar cell absorber. *Appl. Phys. Lett.* **104**, 063903 (2014).
32. Brandt, R. E., Stevanović, V., Ginley, D. S. & Buonassisi, T. Identifying defect-tolerant semiconductors with high minority-carrier lifetimes: beyond hybrid lead halide perovskites. *MRS Commun.* **5**, 265–275 (2015).
33. Zakutayev, A. *et al.* Defect Tolerant Semiconductors for Solar Energy Conversion. *J. Phys. Chem. Lett.* **5**, 1117–1125 (2014).

34. Cohen, A., Egger, D. A., Rappe, A. M. & Kronik, L. Breakdown of the Static Picture of Defect Energetics in Halide Perovskites: The Case of the Br Vacancy in CsPbBr₃. *J. Phys. Chem. Lett.* **10**, 4490–4498 (2019).
35. Futscher, M. H. & Deibel, C. Defect Spectroscopy in Halide Perovskites Is Dominated by Ionic Rather than Electronic Defects. *ACS Energy Lett.* **7**, 140–144 (2022).
36. Heo, S. *et al.* Deep level trapped defect analysis in CH₃NH₃PbI₃ perovskite solar cells by deep level transient spectroscopy. *Energy Environ. Sci.* **10**, 1128–1133 (2017).
37. Yang, W. S. *et al.* Iodide management in formamidinium-lead-halide-based perovskite layers for efficient solar cells. *Science* **356**, 1376–1379 (2017).
38. Keeble, D. J. *et al.* Identification of lead vacancy defects in lead halide perovskites. *Nat. Commun.* **12**, 5566 (2021).
39. Zhang, X., Turiansky, M. E., Shen, J.-X. & Van de Walle, C. G. Defect tolerance in halide perovskites: A first-principles perspective. *J. Appl. Phys.* **131**, 090901 (2022).
40. Kim, S., Márquez, J. A., Unold, T. & Walsh, A. Upper limit to the photovoltaic efficiency of imperfect crystals from first principles. *Energy Environ. Sci.* **13**, 1481–1491 (2020).
41. Shockley, W. & Read, W. T. Statistics of the Recombinations of Holes and Electrons. *Phys. Rev.* **87**, 835–842 (1952).
42. Stoneham, A. M. Non-radiative transitions in semiconductors. *Rep. Prog. Phys.* **44**, 1251 (1981).
43. Jaramillo, R. *et al.* Transient terahertz photoconductivity measurements of minority-carrier lifetime in tin sulfide thin films: Advanced metrology for an early stage photovoltaic material. *J. Appl. Phys.* **119**, 035101 (2016).
44. Brandt, R. E. *et al.* Searching for “Defect-Tolerant” Photovoltaic Materials: Combined Theoretical and Experimental Screening. *Chem. Mater.* **29**, 4667–4674 (2017).

45. Rondiya, S. R., Jagt, R. A., MacManus-Driscoll, J. L., Walsh, A. & Hoye, R. L. Z. Self-trapping in bismuth-based semiconductors: Opportunities and challenges from optoelectronic devices to quantum technologies. *Appl. Phys. Lett.* **119**, 220501 (2021).
46. Wu, B. *et al.* Strong self-trapping by deformation potential limits photovoltaic performance in bismuth double perovskite. *Sci. Adv.* **7**, eabd3160 (2021).
47. Buizza, L. R. V. & Herz, L. M. Polarons and Charge Localization in Metal-Halide Semiconductors for Photovoltaic and Light-Emitting Devices. *Adv. Mater.* **33**, 2007057 (2021).
48. Kavanagh, S. R., Scanlon, D. O., Walsh, A. & Freysoldt, C. Impact of metastable defect structures on carrier recombination in solar cells. *Faraday Discuss.* **239**, 339–356 (2022).
49. Alkauskas, A., Yan, Q. & Van de Walle, C. G. First-principles theory of nonradiative carrier capture via multiphonon emission. *Phys. Rev. B* **90**, 075202 (2014).
50. Nenon, D. P. *et al.* Design Principles for Trap-Free CsPbX₃ Nanocrystals: Enumerating and Eliminating Surface Halide Vacancies with Softer Lewis Bases. *J. Am. Chem. Soc.* **140**, 17760–17772 (2018).
51. Wang, X., Kavanagh, S. R., Scanlon, D. O. & Walsh, A. Upper efficiency limit of Sb₂Se₃ solar cells. *Joule* (2024) doi:10.1016/j.joule.2024.05.004.
52. Kim, S., Park, J.-S. & Walsh, A. Identification of Killer Defects in Kesterite Thin-Film Solar Cells. *ACS Energy Lett.* **3**, 496–500 (2018).
53. Kavanagh, S. R., Walsh, A. & Scanlon, D. O. Rapid Recombination by Cadmium Vacancies in CdTe. *ACS Energy Lett.* **6**, 1392–1398 (2021).
54. Yang, J.-H., Shi, L., Wang, L.-W. & Wei, S.-H. Non-Radiative Carrier Recombination Enhanced by Two-Level Process: A First-Principles Study. *Sci. Rep.* **6**, 21712 (2016).
55. Du, M.-H. Density Functional Calculations of Native Defects in CH₃NH₃PbI₃: Effects of Spin–Orbit Coupling and Self-Interaction Error. *J. Phys. Chem. Lett.* **6**, 1461–1466 (2015).

56. Park, J. S., Kim, S., Xie, Z. & Walsh, A. Point defect engineering in thin-film solar cells. *Nat. Rev. Mater.* **3**, 194–210 (2018).
57. Yang, J.-H., Yin, W.-J., Park, J.-S., Ma, J. & Wei, S.-H. Review on first-principles study of defect properties of CdTe as a solar cell absorber. *Semicond. Sci. Technol.* **31**, 083002 (2016).
58. Ma, J. *et al.* Dependence of the minority-carrier lifetime on the stoichiometry of CdTe using time-resolved photoluminescence and first-principles calculations. *Phys. Rev. Lett.* **111**, 067402 (2013).
59. Mosquera-Lois, I., Kavanagh, S. R., Walsh, A. & Scanlon, D. O. Identifying the ground state structures of point defects in solids. *npj Comput. Mater.* **9**, 1–11 (2023).
60. Mosquera-Lois, I. & Kavanagh, S. R. In search of hidden defects. *Matter* **4**, 2602–2605 (2021).
61. Freysoldt, C. *et al.* First-principles calculations for point defects in solids. *Rev. Mod. Phys.* **86**, 253–305 (2014).
62. Mosquera-Lois, I., Kavanagh, S. R., Klarbring, J., Tolborg, K. & Walsh, A. Imperfections are not 0 K: free energy of point defects in crystals. *Chem. Soc. Rev.* **52**, 5812–5826 (2023).
63. Broberg, D. *et al.* PyCDT: A Python toolkit for modeling point defects in semiconductors and insulators. *Comput. Phys. Commun.* **226**, 165–179 (2018).
64. Shen, J.-X. & Varley, J. pymatgen-analysis-defects: A Python package for analyzing point defects in crystalline materials. *J. Open Source Softw.* **9**, 5941 (2024).
65. Squires, A. G., Scanlon, D. O. & Morgan, B. J. py-sc-fermi: self-consistent Fermi energies and defect concentrations from electronic structure calculations. *J. Open Source Softw.* **8**, 4962 (2023).
66. Mosquera-Lois, I., Kavanagh, S. R., Walsh, A. & Scanlon, D. O. ShakeNBreak: Navigating the defect configurational landscape. *J. Open Source Softw.* **7**, 4817 (2022).

67. Neilson, W. D. & Murphy, S. T. DefAP: A Python code for the analysis of point defects in crystalline solids. *Comput. Mater. Sci.* **210**, 111434 (2022).
68. Goyal, A., Gorai, P., Peng, H., Lany, S. & Stevanović, V. A computational framework for automation of point defect calculations. *Comput. Mater. Sci.* **130**, 1–9 (2017).
69. Kavanagh, S. R. *et al.* doped: Python toolkit for robust and repeatable charged defect supercell calculations. *J. Open Source Softw.* **9**, 6433 (2024).
70. Kumagai, Y., Tsunoda, N., Takahashi, A. & Oba, F. Insights into oxygen vacancies from high-throughput first-principles calculations. *Phys. Rev. Mater.* **5**, 123803 (2021).
71. Zhang, X., Turiansky, M. E. & Van de Walle, C. G. Correctly Assessing Defect Tolerance in Halide Perovskites. *J. Phys. Chem. C* **124**, 6022–6027 (2020).
72. Zhang, X., Shen, J.-X., Turiansky, M. E. & Walle, C. G. V. de. Hidden role of Bi incorporation in nonradiative recombination in methylammonium lead iodide. *J. Mater. Chem. A* **8**, 12964–12967 (2020).
73. Shi, L. & Wang, L.-W. Ab initio Calculations of Deep-Level Carrier Nonradiative Recombination Rates in Bulk Semiconductors. *Phys. Rev. Lett.* **109**, 245501 (2012).
74. Kim, S., Hood, S. N. & Walsh, A. Anharmonic lattice relaxation during nonradiative carrier capture. *Phys. Rev. B* **100**, 041202 (2019).
75. Kim, S., Hood, S. N., Gerwen, P. van, Whalley, L. D. & Walsh, A. CarrierCapture.jl: Anharmonic Carrier Capture. *J. Open Source Softw.* **5**, 2102 (2020).
76. Turiansky, M. E. *et al.* Nonrad: Computing nonradiative capture coefficients from first principles. *Comput. Phys. Commun.* **267**, 108056 (2021).
77. Qiao, L., Fang, W.-H., Long, R. & Prezhdo, O. V. Atomic Model for Alkali Metal Passivation of Point Defects at Perovskite Grain Boundaries. *ACS Energy Lett.* **5**, 3813–3820 (2020).
78. Zhao, K., Xiang, H., Zhu, R., Liu, C. & Jia, Y. Passivation principle of deep-level defects: a study of SnZn defects in kesterites for high-efficient solar cells. *J. Mater. Chem. A* **10**, 2849–2855 (2022).

79. Cai, Z. *et al.* Active Passivation of Anion Vacancies in Antimony Selenide Film for Efficient Solar Cells. *Adv. Mater.* 2404826 (2024) doi:10.1002/adma.202404826.
80. Du, Y. *et al.* Defect Engineering in Earth-Abundant $\text{Cu}_2\text{ZnSn}(\text{S,Se})_4$ Photovoltaic Materials via Ga^{3+} -Doping for over 12% Efficient Solar Cells. *Adv. Funct. Mater.* **31**, 2010325 (2021).
81. Wilson, J. N., Frost, J. M., Wallace, S. K. & Walsh, A. Dielectric and ferroic properties of metal halide perovskites. *APL Mater.* **7**, 010901 (2019).
82. Adinolfi, V. *et al.* The In-Gap Electronic State Spectrum of Methylammonium Lead Iodide Single-Crystal Perovskites. *Adv. Mater.* **28**, 3406–3410 (2016).
83. Du, M. H. Efficient carrier transport in halide perovskites: theoretical perspectives. *J. Mater. Chem. A* **2**, 9091–9098 (2014).
84. Whalley, L. D. *et al.* Giant Huang–Rhys Factor for Electron Capture by the Iodine Interstitial in Perovskite Solar Cells. *J. Am. Chem. Soc.* **143**, 9123–9128 (2021).
85. Zhang, J., Zhang, X., Turiansky, M. E. & Van de Walle, C. G. Iodine Vacancies do not Cause Nonradiative Recombination in Halide Perovskites. *PRX Energy* **2**, 013008 (2023).
86. Zhang, S. B., Wei, S.-H., Zunger, A. & Katayama-Yoshida, H. Defect physics of the CuInSe_2 chalcopyrite semiconductor. *Phys. Rev. B* **57**, 9642–9656 (1998).
87. Huang, Y.-T., Kavanagh, S. R., Scanlon, D. O., Walsh, A. & Hoye, R. L. Z. Perovskite-inspired materials for photovoltaics and beyond—from design to devices. *Nanotechnology* **32**, 132004 (2021).
88. Nenon, D. P. *et al.* Design Principles for Trap-Free CsPbX_3 Nanocrystals: Enumerating and Eliminating Surface Halide Vacancies with Softer Lewis Bases. *J. Am. Chem. Soc.* **140**, 17760–17772 (2018).
89. Kim, J., Chung, C.-H. & Hong, K.-H. Understanding of the formation of shallow level defects from the intrinsic defects of lead tri-halide perovskites. *Phys. Chem. Chem. Phys.* **18**, 27143–27147 (2016).

90. Ganose, A. M., Scanlon, D. O., Walsh, A. & Hoye, R. L. Z. The defect challenge of wide-bandgap semiconductors for photovoltaics and beyond. *Nat. Commun.* **13**, 4715 (2022).
91. Zhang, X. & Wei, S.-H. Origin of Efficiency Enhancement by Lattice Expansion in Hybrid-Perovskite Solar Cells. *Phys. Rev. Lett.* **128**, 136401 (2022).
92. Zhang, X., Turiansky, M. E., Shen, J.-X. & Van de Walle, C. G. Iodine interstitials as a cause of nonradiative recombination in hybrid perovskites. *Phys. Rev. B* **101**, 140101 (2020).
93. Zhang, X., Shen, J. X., Turiansky, M. E. & Van de Walle, C. G. Minimizing hydrogen vacancies to enable highly efficient hybrid perovskites. *Nat. Mater.* **20**, 971–976 (2021).
94. Stoumpos, C. C., Malliakas, C. D. & Kanatzidis, M. G. Semiconducting tin and lead iodide perovskites with organic cations: Phase transitions, high mobilities, and near-infrared photoluminescent properties. *Inorg. Chem.* **52**, 9019–9038 (2013).
95. Mitzi, D. B., Feild, C. A., Schlesinger, Z. & Laibowitz, R. B. Transport, Optical, and Magnetic Properties of the Conducting Halide Perovskite $\text{CH}_3\text{NH}_3\text{SnI}_3$. *J. Solid State Chem.* **114**, 159–163 (1995).
96. Walsh, A., Scanlon, D. O., Chen, S., Gong, X. G. & Wei, S.-H. Self-Regulation Mechanism for Charged Point Defects in Hybrid Halide Perovskites. *Angew. Chem.* **127**, 1811–1814 (2015).
97. Yang, J.-H., Yin, W.-J., Park, J.-S. & Wei, S.-H. Self-regulation of charged defect compensation and formation energy pinning in semiconductors. *Sci. Rep.* **5**, 16977 (2015).
98. Zhu, H. *et al.* Screening in crystalline liquids protects energetic carriers in hybrid perovskites. *Science* **353**, 1409–1413 (2016).
99. Miyata, K. *et al.* Large polarons in lead halide perovskites. *Sci. Adv.* **3**, e1701217 (2017).
100. Miyata, K. & Zhu, X.-Y. Ferroelectric large polarons. *Nat. Mater.* **17**, 379–381 (2018).
101. Herz, L. M. Charge-Carrier Mobilities in Metal Halide Perovskites: Fundamental Mechanisms and Limits. *ACS Energy Lett.* **2**, 1539–1548 (2017).
102. Stranks, S. D. *et al.* Electron-Hole Diffusion Lengths Exceeding 1 Micrometer in an Organometal Trihalide Perovskite Absorber. *Science* **342**, 341–344 (2013).

103. Chu, W., Zheng, Q., Prezhdo, O. V., Zhao, J. & Saidi, W. A. Low-frequency lattice phonons in halide perovskites explain high defect tolerance toward electron-hole recombination. *Sci. Adv.* **6**, eaaw7453 (2020).
104. Chu, W., Saidi, W. A., Zhao, J. & Prezhdo, O. V. Soft Lattice and Defect Covalency Rationalize Tolerance of β -CsPbI₃ Perovskite Solar Cells to Native Defects. *Angew. Chem. Int. Ed.* **59**, 6435–6441 (2020).
105. Spina, M. *et al.* Mechanical signatures of degradation of the photovoltaic perovskite CH₃NH₃PbI₃ upon water vapor exposure. *Appl. Phys. Lett.* **110**, 121903 (2017).
106. Fukuhara, M. & Yamauchi, I. Temperature dependence of the elastic moduli, dilational and shear internal frictions and acoustic wave velocity for alumina, (Y)TZP and β' -sialon ceramics. *J. Mater. Sci.* **28**, 4681–4688 (1993).
107. Leguy, A. M. A. *et al.* Dynamic disorder, phonon lifetimes, and the assignment of modes to the vibrational spectra of methylammonium lead halide perovskites. *Phys. Chem. Chem. Phys.* **18**, 27051–27066 (2016).
108. Frost, J. M. Calculating polaron mobility in halide perovskites. *Phys. Rev. B* **96**, 195202 (2017).
109. Kirchartz, T., Markvart, T., Rau, U. & Egger, D. A. Impact of Small Phonon Energies on the Charge-Carrier Lifetimes in Metal-Halide Perovskites. *J. Phys. Chem. Lett.* **9**, 939–946 (2018).
110. Wang, S. *et al.* Effective lifetime of non-equilibrium carriers in semiconductors from non-adiabatic molecular dynamics simulations. *Nat. Comput. Sci.* **2**, 486–493 (2022).
111. Lang, F. *et al.* Radiation Hardness and Self-Healing of Perovskite Solar Cells. *Adv. Mater.* **28**, 8726–8731 (2016).
112. Andričević, P. *et al.* Kilogram-Scale Crystallography of Halide Perovskites for Gamma-Rays Dose Rate Measurements. *Adv. Sci.* **8**, 2001882 (2021).

113. Wei, H. *et al.* Sensitive X-ray detectors made of methylammonium lead tribromide perovskite single crystals. *Nat. Photonics* **10**, 333–339 (2016).
114. Domanski, K. *et al.* Migration of cations induces reversible performance losses over day/night cycling in perovskite solar cells. *Energy Environ. Sci.* **10**, 604–613 (2017).
115. Bag, M. *et al.* Kinetics of Ion Transport in Perovskite Active Layers and Its Implications for Active Layer Stability. *J. Am. Chem. Soc.* **137**, 13130–13137 (2015).
116. Nie, W. *et al.* Light-activated photocurrent degradation and self-healing in perovskite solar cells. *Nat. Commun.* **7**, 11574 (2016).
117. Yadav, P., Prochowicz, D., Alharbi, E. A., Zakeeruddin, S. M. & Grätzel, M. Intrinsic and interfacial kinetics of perovskite solar cells under photo and bias-induced degradation and recovery. *J. Mater. Chem. C* **5**, 7799–7805 (2017).
118. Wang, C. *et al.* Self-Healing Behavior of the Metal Halide Perovskites and Photovoltaics. *Small* **20**, 2307645 (2024).
119. Yadavalli, S. K., Dai, Z., Zhou, H., Zhou, Y. & Padture, N. P. Facile healing of cracks in organic–inorganic halide perovskite thin films. *Acta Mater.* **187**, 112–121 (2020).
120. Al-Handawi, M. B. *et al.* Autonomous Reconstitution of Fractured Hybrid Perovskite Single Crystals. *Adv. Mater.* **34**, 2109374 (2022).
121. Guillemoles, J.-F., Rau, U., Kronik, L., Schock, H.-W. & Cahen, D. Cu(In,Ga)Se₂ Solar Cells: Device Stability Based on Chemical Flexibility. *Adv. Mater.* **11**, 957–961 (1999).
122. Rakita, Y., Lubomirsky, I. & Cahen, D. When defects become ‘dynamic’: halide perovskites: a new window on materials? *Mater. Horiz.* **6**, 1297–1305 (2019).
123. Zhou, Z. *et al.* Methylamine-Gas-Induced Defect-Healing Behavior of CH₃NH₃PbI₃ Thin Films for Perovskite Solar Cells. *Angew. Chem. Int. Ed.* **54**, 9705–9709 (2015).
124. de Mello, J. C., Wittmann, H. F. & Friend, R. H. An improved experimental determination of external photoluminescence quantum efficiency. *Adv. Mater.* **9**, 230–232 (1997).

125. *Advanced Time-Correlated Single Photon Counting Applications*. vol. 111 (Springer International Publishing, Cham, 2015).
126. Berera, R., van Grondelle, R. & Kennis, J. T. M. Ultrafast transient absorption spectroscopy: principles and application to photosynthetic systems. *Photosynth. Res.* **101**, 105–118 (2009).
127. Guthrey, H. & Moseley, J. A Review and Perspective on Cathodoluminescence Analysis of Halide Perovskites. *Adv. Energy Mater.* **10**, 1903840 (2020).
128. Richter, J. M. *et al.* Enhancing photoluminescence yields in lead halide perovskites by photon recycling and light out-coupling. *Nat. Commun.* **7**, 13941 (2016).
129. Sadhanala, A. *et al.* Preparation of Single-Phase Films of $\text{CH}_3\text{NH}_3\text{Pb}(\text{I}_{1-x}\text{Br}_x)_3$ with Sharp Optical Band Edges. *J. Phys. Chem. Lett.* **5**, 2501–2505 (2014).
130. Kronik, L. & Shapira, Y. Surface photovoltage phenomena: theory, experiment, and applications. *Surf. Sci. Rep.* **37**, 1–206 (1999).
131. van Gorkom, B. T., van der Pol, T. P. A., Datta, K., Wienk, M. M. & Janssen, R. A. J. Revealing defective interfaces in perovskite solar cells from highly sensitive sub-bandgap photocurrent spectroscopy using optical cavities. *Nat. Commun.* **13**, 349 (2022).
132. Le Corre, V. M. *et al.* Revealing Charge Carrier Mobility and Defect Densities in Metal Halide Perovskites via Space-Charge-Limited Current Measurements. *ACS Energy Lett.* **6**, 1087–1094 (2021).
133. Lang, D. V. Deep-level transient spectroscopy: A new method to characterize traps in semiconductors. *J. Appl. Phys.* **45**, 3023–3032 (1974).
134. Losee, D. L. Admittance spectroscopy of deep impurity levels: ZnTe Schottky barriers. *Appl. Phys. Lett.* **21**, 54–56 (1972).
135. Leon, C., Le Gall, S., Gueunier-Farret, M.-E. & Kleider, J.-P. How to perform admittance spectroscopy and DLTS in multijunction solar cells. *Sol. Energy Mater. Sol. Cells* **240**, 111699 (2022).

136. Hoye, R. L. Z. *et al.* The Role of Dimensionality on the Optoelectronic Properties of Oxide and Halide Perovskites, and their Halide Derivatives. *Adv. Energy Mater.* **12**, 2100499 (2022).
137. Dunlap-Shohl, W. A., Hill, I. G., Yan, Y. & Mitzi, D. B. Photovoltaic Effect in Indium(I) Iodide Thin Films. *Chem. Mater.* **30**, 8226–8232 (2018).
138. López-Fernández, I. *et al.* Lead-Free Halide Perovskite Materials and Optoelectronic Devices: Progress and Prospective. *Adv. Funct. Mater.* **34**, 2307896 (2024).
139. Ganose, A. M., Savory, C. N. & Scanlon, D. O. Beyond methylammonium lead iodide: prospects for the emergent field of ns² containing solar absorbers. *Chem. Commun.* **53**, 20–44 (2016).
140. Glück, N. & Bein, T. Prospects of lead-free perovskite-inspired materials for photovoltaic applications. *Energy Environ. Sci.* **13**, 4691–4716 (2020).
141. Cao, J. & Yan, F. Recent progress in tin-based perovskite solar cells. *Energy Environ. Sci.* **14**, 1286–1325 (2021).
142. Tai, Q. *et al.* Antioxidant Grain Passivation for Air-Stable Tin-Based Perovskite Solar Cells. *Angew. Chem. Int. Ed.* **58**, 806–810 (2019).
143. Hasan, S. A. U., Lee, D. S., Im, S. H. & Hong, K.-H. Present Status and Research Prospects of Tin-based Perovskite Solar Cells. *Sol. RRL* **4**, 1900310 (2020).
144. Krishnamoorthy, T. *et al.* Lead-free germanium iodide perovskite materials for photovoltaic applications. *J. Mater. Chem. A* **3**, 23829–23832 (2015).
145. Chiara, R., Morana, M. & Malavasi, L. Germanium-Based Halide Perovskites: Materials, Properties, and Applications. *ChemPlusChem* **86**, 879–888 (2021).
146. Zhang, X. *et al.* Active-layer evolution and efficiency improvement of (CH₃NH₃)₃Bi₂I₉-based solar cell on TiO₂-deposited ITO substrate. *Nano Res.* **9**, 2921–2930 (2016).
147. Jain, S. M. *et al.* An effective approach of vapour assisted morphological tailoring for reducing metal defect sites in lead-free, (CH₃NH₃)₃Bi₂I₉ bismuth-based perovskite solar cells for improved performance and long-term stability. *Nano Energy* **49**, 614–624 (2018).

148. Park, B. *et al.* Bismuth Based Hybrid Perovskites $A_3Bi_2I_9$ (A: Methylammonium or Cesium) for Solar Cell Application. *Adv. Mater.* **27**, 6806–6813 (2015).
149. Bai, F. *et al.* Lead-free, air-stable ultrathin $Cs_3Bi_2I_9$ perovskite nanosheets for solar cells. *Sol. Energy Mater. Sol. Cells* **184**, 15–21 (2018).
150. Correa-Baena, J.-P. *et al.* A -Site Cation in Inorganic $A_3Sb_2I_9$ Perovskite Influences Structural Dimensionality, Exciton Binding Energy, and Solar Cell Performance. *Chem. Mater.* **30**, 3734–3742 (2018).
151. Singh, A. *et al.* Panchromatic heterojunction solar cells for Pb-free all-inorganic antimony based perovskite. *Chem. Eng. J.* **419**, 129424 (2021).
152. Singh, A. *et al.* Photovoltaic Performance of Vapor-Assisted Solution-Processed Layer Polymorph of $Cs_3Sb_2I_9$. *ACS Appl. Mater. Interfaces* **10**, 2566–2573 (2018).
153. Ke, W. *et al.* Enhanced photovoltaic performance and stability with a new type of hollow 3D perovskite $\{en\}FASnI_3$. *Sci. Adv.* **3**, e1701293 (2017).
154. Lee, S. J. *et al.* Fabrication of Efficient Formamidinium Tin Iodide Perovskite Solar Cells through SnF_2 –Pyrazine Complex. *J. Am. Chem. Soc.* **138**, 3974–3977 (2016).
155. Koh, T. M. *et al.* Formamidinium tin-based perovskite with low E_g for photovoltaic applications. *J. Mater. Chem. A* **3**, 14996–15000 (2015).
156. Yu, B. *et al.* Heterogeneous 2D/3D Tin-Halides Perovskite Solar Cells with Certified Conversion Efficiency Breaking 14%. *Adv. Mater.* **33**, 2102055 (2021).
157. Shao, S. *et al.* Highly Reproducible Sn-Based Hybrid Perovskite Solar Cells with 9% Efficiency. *Adv. Energy Mater.* **8**, 1702019 (2018).
158. Dixit, H., Punetha, D. & Pandey, S. K. Improvement in performance of lead free inverted perovskite solar cell by optimization of solar parameters. *Optik* **179**, 969–976 (2019).
159. Shi, Y., Zhu, Z., Miao, D., Ding, Y. & Mi, Q. Interfacial Dipoles Boost Open-Circuit Voltage of Tin Halide Perovskite Solar Cells. *ACS Energy Lett.* **9**, 1895–1897 (2024).

160. Cui, D. *et al.* Making Room for Growing Oriented FASnI₃ with Large Grains via Cold Precursor Solution. *Adv. Funct. Mater.* **31**, 2100931 (2021).
161. Wang, C. *et al.* Self-Repairing Tin-Based Perovskite Solar Cells with a Breakthrough Efficiency Over 11%. *Adv. Mater.* **32**, 1907623 (2020).
162. Meng, X. *et al.* Surface-Controlled Oriented Growth of FASnI₃ Crystals for Efficient Lead-free Perovskite Solar Cells. *Joule* **4**, 902–912 (2020).
163. Ke, W. *et al.* TiO₂–ZnS Cascade Electron Transport Layer for Efficient Formamidinium Tin Iodide Perovskite Solar Cells. *J. Am. Chem. Soc.* **138**, 14998–15003 (2016).
164. Li, F. *et al.* A Cation-Exchange Approach for the Fabrication of Efficient Methylammonium Tin Iodide Perovskite Solar Cells. *Angew. Chem. Int. Ed.* **58**, 6688–6692 (2019).
165. Xu, F., Wei, H. & Cao, B. A hot phonon bottleneck observed upon incorporation of SnF₂ to MASnI₃ films and its possible role in increasing photocarrier diffusion length. *J. Appl. Phys.* **135**, 133102 (2024).
166. Ke, W. *et al.* Efficient Lead-Free Solar Cells Based on Hollow {en}MASnI₃ Perovskites. *J. Am. Chem. Soc.* **139**, 14800–14806 (2017).
167. Ji, L. *et al.* Regulating crystallization dynamics and crystal orientation of methylammonium tin iodide enables high-efficiency lead-free perovskite solar cells. *Nanoscale* **14**, 1219–1225 (2022).
168. Ye, T. *et al.* Ambient-Air-Stable Lead-Free CsSnI₃ Solar Cells with Greater than 7.5% Efficiency. *J. Am. Chem. Soc.* **143**, 4319–4328 (2021).
169. Wang, Y. *et al.* Convenient preparation of CsSnI₃ quantum dots, excellent stability, and the highest performance of lead-free inorganic perovskite solar cells so far. *J. Mater. Chem. A* **7**, 7683–7690 (2019).
170. Marshall, K. P., Walker, M., Walton, R. I. & Hatton, R. A. Enhanced stability and efficiency in hole-transport-layer-free CsSnI₃ perovskite photovoltaics. *Nat. Energy* **1**, 16178 (2016).

171. Ye, T. *et al.* Localized Electron Density Engineering for Stabilized B- γ CsSnI₃-Based Perovskite Solar Cells with Efficiencies >10%. *ACS Energy Lett.* **6**, 1480–1489 (2021).
172. Zhang, W. *et al.* Organic-Free and Lead-Free Perovskite Solar Cells with Efficiency over 11%. *Adv. Energy Mater.* **12**, 2202491 (2022).
173. Zhang, Z. *et al.* Over 12% efficient CsSnI₃ perovskite solar cells enabled by surface post-treatment with bi-functional polar molecules. *Chem. Eng. J.* **490**, 151561 (2024).
174. Song, T.-B., Yokoyama, T., Aramaki, S. & Kanatzidis, M. G. Performance Enhancement of Lead-Free Tin-Based Perovskite Solar Cells with Reducing Atmosphere-Assisted Dispersible Additive. *ACS Energy Lett.* **2**, 897–903 (2017).
175. Dai, L. *et al.* Single-Crystal Nanowire Cesium Tin Triiodide Perovskite Solar Cell. *Small* **19**, 2208062 (2023).
176. Huang, P.-C., Yang, W.-C. & Lee, M.-W. AgBiS₂ Semiconductor-Sensitized Solar Cells. *J. Phys. Chem. C* **117**, 18308–18314 (2013).
177. Wang, Y. *et al.* Cation disorder engineering yields AgBiS₂ nanocrystals with enhanced optical absorption for efficient ultrathin solar cells. *Nat. Photonics* **16**, 235–241 (2022).
178. Burgués-Ceballos, I., Wang, Y., Akgul, M. Z. & Konstantatos, G. Colloidal AgBiS₂ nanocrystals with reduced recombination yield 6.4% power conversion efficiency in solution-processed solar cells. *Nano Energy* **75**, 104961 (2020).
179. Zhou, S. *et al.* Preparation and Photovoltaic Properties of Ternary AgBiS₂ Quantum Dots Sensitized TiO₂ Nanorods Photoanodes by Electrochemical Atomic Layer Deposition. *J. Electrochem. Soc.* **163**, D63–D67 (2016).
180. Bernechea, M. *et al.* Solution-processed solar cells based on environmentally friendly AgBiS₂ nanocrystals. *Nat. Photonics* **10**, 521–525 (2016).
181. Li, X. *et al.* Thin film AgBiS₂ solar cells with over 10 % power conversion efficiency enabled by vapor-assisted solution process treatment. *Chem. Eng. J.* **495**, 153328 (2024).

182. Sfaelou, S., Raptis, D., Dracopoulos, V. & Lianos, P. BiOI solar cells. *RSC Adv.* **5**, 95813–95816 (2015).
183. Wang, K., Jia, F., Zheng, Z. & Zhang, L. Crossed BiOI flake array solar cells. *Electrochem. Commun.* **12**, 1764–1767 (2010).
184. Hoye, R. L. Z. *et al.* Strongly Enhanced Photovoltaic Performance and Defect Physics of Air-Stable Bismuth Oxyiodide (BiOI). *Adv. Mater.* **29**, 1702176 (2017).
185. Welch, A. W. *et al.* CuSbSe₂ photovoltaic devices with 3% efficiency. *Appl. Phys. Express* **8**, 082301 (2015).
186. Welch, A. W. *et al.* Trade-Offs in Thin Film Solar Cells with Layered Chalcostibite Photovoltaic Absorbers. *Adv. Energy Mater.* **7**, 1601935 (2017).
187. Banu, S., Ahn, S. J., Ahn, S. K., Yoon, K. & Cho, A. Fabrication and characterization of cost-efficient CuSbS₂ thin film solar cells using hybrid inks. *Sol. Energy Mater. Sol. Cells* **151**, 14–23 (2016).
188. Septina, W., Ikeda, S., Iga, Y., Harada, T. & Matsumura, M. Thin film solar cell based on CuSbS₂ absorber fabricated from an electrochemically deposited metal stack. *Thin Solid Films* **550**, 700–704 (2014).
189. Wang, S. *et al.* A Novel Multi-Sulfur Source Collaborative Chemical Bath Deposition Technology Enables 8%-Efficiency Sb₂S₃ Planar Solar Cells. *Adv. Mater.* **34**, 2206242 (2022).
190. Chang, J. A. *et al.* High-Performance Nanostructured Inorganic–Organic Heterojunction Solar Cells. *Nano Lett.* **10**, 2609–2612 (2010).
191. Choi, Y. C., Lee, D. U., Noh, J. H., Kim, E. K. & Seok, S. I. Highly Improved Sb₂S₃ Sensitized-Inorganic–Organic Heterojunction Solar Cells and Quantification of Traps by Deep-Level Transient Spectroscopy. *Adv. Funct. Mater.* **24**, 3587–3592 (2014).
192. Nezu, S. *et al.* Light Soaking and Gas Effect on Nanocrystalline TiO₂/Sb₂S₃/CuSCN Photovoltaic Cells following Extremely Thin Absorber Concept. *J. Phys. Chem. C* **114**, 6854–6859 (2010).

193. Chang, J. A. *et al.* Panchromatic Photon-Harvesting by Hole-Conducting Materials in Inorganic–Organic Heterojunction Sensitized-Solar Cell through the Formation of Nanostructured Electron Channels. *Nano Lett.* **12**, 1863–1867 (2012).
194. Itzhaik, Y., Niitsoo, O., Page, M. & Hodes, G. Sb₂S₃-Sensitized Nanoporous TiO₂ Solar Cells. *J. Phys. Chem. C* **113**, 4254–4256 (2009).
195. Im, S. H. *et al.* Toward Interaction of Sensitizer and Functional Moieties in Hole-Transporting Materials for Efficient Semiconductor-Sensitized Solar Cells. *Nano Lett.* **11**, 4789–4793 (2011).
196. Li, Z. *et al.* 9.2%-efficient core-shell structured antimony selenide nanorod array solar cells. *Nat. Commun.* **10**, 125 (2019).
197. Kolay, A. *et al.* New Antimony Selenide/Nickel Oxide Photocathode Boosts the Efficiency of Graphene Quantum-Dot Co-Sensitized Solar Cells. *ACS Appl. Mater. Interfaces* **9**, 34915–34926 (2017).
198. Choi, Y. C. *et al.* Sb₂Se₃-Sensitized Inorganic–Organic Heterojunction Solar Cells Fabricated Using a Single-Source Precursor. *Angew. Chem. Int. Ed.* **53**, 1329–1333 (2014).
199. Duan, Z. *et al.* Sb₂Se₃ Thin-Film Solar Cells Exceeding 10% Power Conversion Efficiency Enabled by Injection Vapor Deposition Technology. *Adv. Mater.* **34**, 2202969 (2022).
200. Leng, M. *et al.* Selenization of Sb₂Se₃ absorber layer: An efficient step to improve device performance of CdS/Sb₂Se₃ solar cells. *Appl. Phys. Lett.* **105**, 083905 (2014).
201. Zhou, Y. *et al.* Thin-film Sb₂Se₃ photovoltaics with oriented one-dimensional ribbons and benign grain boundaries. *Nat. Photonics* **9**, 409–415 (2015).
202. Messina, S., Nair, M. T. S. & Nair, P. K. Antimony Selenide Absorber Thin Films in All-Chemically Deposited Solar Cells. *J. Electrochem. Soc.* **156**, H327 (2009).
203. Choi, Y. C. *et al.* Efficient Inorganic–Organic Heterojunction Solar Cells Employing Sb₂(S_x/Se_{1-x})₃ Graded-Composition Sensitizers. *Adv. Energy Mater.* **4**, 1301680 (2014).

204. Tang, R. *et al.* Hydrothermal deposition of antimony selenosulfide thin films enables solar cells with 10% efficiency. *Nat. Energy* **5**, 587–595 (2020).
205. Wu, C. *et al.* Interfacial Engineering by Indium-Doped CdS for High Efficiency Solution Processed $\text{Sb}_2(\text{S}_{1-x}\text{Se}_x)_3$ Solar Cells. *ACS Appl. Mater. Interfaces* **11**, 3207–3213 (2019).
206. Wang, X. *et al.* Manipulating the Electrical Properties of $\text{Sb}_2(\text{S,Se})_3$ Film for High-Efficiency Solar Cell. *Adv. Energy Mater.* **10**, 2002341 (2020).
207. Zhao, Y. *et al.* Regulating Energy Band Alignment via Alkaline Metal Fluoride Assisted Solution Post-Treatment Enabling $\text{Sb}_2(\text{S,Se})_3$ Solar Cells with 10.7% Efficiency. *Adv. Energy Mater.* **12**, 2103015 (2022).
208. Chen, X. *et al.* Solvent-Assisted Hydrothermal Deposition Approach for Highly-Efficient $\text{Sb}_2(\text{S,Se})_3$ Thin-Film Solar Cells. *Adv. Energy Mater.* **13**, 2300391 (2023).
209. Mohan, R. Green bismuth. *Nat. Chem.* **2**, 336–336 (2010).
210. Huang, Y.-T. *et al.* Strong absorption and ultrafast localisation in NaBiS_2 nanocrystals with slow charge-carrier recombination. *Nat. Commun.* **13**, 4960 (2022).
211. Lal, S. *et al.* The Role of Chemical Composition in Determining the Charge-Carrier Dynamics in $(\text{AgI})_x(\text{BiI}_3)_y$ Rudorffites. *Adv. Funct. Mater.* 2315942 (2024)
doi:10.1002/adfm.202315942.
212. Jia, Z. *et al.* Charge-Carrier Dynamics of Solution-Processed Antimony- and Bismuth-Based Chalcogenide Thin Films. *ACS Energy Lett.* **8**, 1485–1492 (2023).
213. Lal, S. *et al.* Bandlike Transport and Charge-Carrier Dynamics in BiOI Films. *J. Phys. Chem. Lett.* **14**, 6620–6629 (2023).
214. Zhao, Y. *et al.* Regulating deposition kinetics via a novel additive-assisted chemical bath deposition technology enables fabrication of 10.57%-efficiency Sb_2Se_3 solar cells. *Energy Environ. Sci.* **15**, 5118–5128 (2022).
215. Chen, X. *et al.* Additive engineering for Sb_2S_3 indoor photovoltaics with efficiency exceeding 17%. Preprint at <https://doi.org/10.48550/arXiv.2406.06807> (2024).

216. Liu, X. *et al.* Grain Engineering of Sb₂S₃ Thin Films to Enable Efficient Planar Solar Cells with High Open-Circuit Voltage. *Adv. Mater.* **36**, 2305841 (2024).
217. Yang, B. *et al.* CuSbS₂ as a Promising Earth-Abundant Photovoltaic Absorber Material: A Combined Theoretical and Experimental Study. *Chem. Mater.* **26**, 3135–3143 (2014).
218. Peccerillo, E. & Durose, K. Copper—antimony and copper—bismuth chalcogenides—Research opportunities and review for solar photovoltaics. *MRS Energy Sustain.* **5**, 9 (2018).
219. Yee, Y. S. *et al.* Copper interstitial recombination centers in Cu₃N. *Phys. Rev. B* **97**, 245201 (2018).
220. Kurchin, R. C., Gorai, P., Buonassisi, T. & Stevanović, V. Structural and Chemical Features Giving Rise to Defect Tolerance of Binary Semiconductors. *Chem. Mater.* **30**, 5583–5592 (2018).
221. Huq, T. N. *et al.* Electronic Structure and Optoelectronic Properties of Bismuth Oxyiodide Robust against Percent-Level Iodine-, Oxygen-, and Bismuth-Related Surface Defects. *Adv. Funct. Mater.* **30**, 1909983 (2020).
222. Shi, H. & Du, M.-H. Shallow halogen vacancies in halide optoelectronic materials. *Phys. Rev. B* **90**, 174103 (2014).
223. Pandey, M. *et al.* Defect-Tolerant Monolayer Transition Metal Dichalcogenides. *Nano Lett.* **16**, 2234–2239 (2016).
224. Pecunia, V., Occhipinti, L. G. & Hoye, R. L. Z. Emerging Indoor Photovoltaic Technologies for Sustainable Internet of Things. *Adv. Energy Mater.* **11**, 2100698 (2021).
225. Bhattarai, S., Sharma, A. & Das, T. D. Efficiency enhancement of perovskite solar cell by using doubly carrier transport layers with a distinct bandgap of MAPbI₃ active layer. *Optik* **224**, 165430 (2020).
226. Zhao, X. *et al.* Macroscopic piezoelectricity of an MAPbI₃ semiconductor and its associated multifunctional device. *Nano Energy* **118**, 108980 (2023).

227. Savory, C. N. & Scanlon, D. O. The complex defect chemistry of antimony selenide. *J. Mater. Chem. A* **7**, 10739–10744 (2019).
228. Hobson, T. D. C., Phillips, L. J., Hutter, O. S., Durose, K. & Major, J. D. Defect properties of Sb₂Se₃ thin film solar cells and bulk crystals. *Appl. Phys. Lett.* **116**, 261101 (2020).
229. Wang, X., Kavanagh, S. R., Scanlon, D. O. & Walsh, A. Four-electron negative-U vacancy defects in antimony selenide. *Phys. Rev. B* **108**, 134102 (2023).
230. Franchini, C., Reticcioli, M., Setvin, M. & Diebold, U. Polarons in materials. *Nat. Rev. Mater.* **6**, 560–586 (2021).
231. Wright, A. D. *et al.* Ultrafast Excited-State Localization in Cs₂AgBiBr₆ Double Perovskite. *J. Phys. Chem. Lett.* **12**, 3352–3360 (2021).
232. McCall, K. M., Stoumpos, C. C., Kostina, S. S., Kanatzidis, M. G. & Wessels, B. W. Strong Electron–Phonon Coupling and Self-Trapped Excitons in the Defect Halide Perovskites A₃M₂I₉ (A = Cs, Rb; M = Bi, Sb). *Chem. Mater.* **29**, 4129–4145 (2017).
233. Scholz, M., Oum, K. & Lenzer, T. Pronounced exciton and coherent phonon dynamics in BiI₃. *Phys. Chem. Chem. Phys.* **20**, 10677–10685 (2018).
234. Buizza, L. R. V. *et al.* Interplay of Structure, Charge-Carrier Localization and Dynamics in Copper-Silver-Bismuth-Halide Semiconductors. *Adv. Funct. Mater.* **32**, 2108392 (2022).
235. Poindexter, J. R. *et al.* High Tolerance to Iron Contamination in Lead Halide Perovskite Solar Cells. *ACS Nano* **11**, 7101–7109 (2017).

Acknowledgements

Y.-T.H. and H.L. arranged alphabetically by surname in byline. I. M.-L. acknowledges Imperial College London for funding from a President’s PhD scholarship. R. L. Z. H., H. L. and J. Y. acknowledge support from a UK Research and Innovation Frontier Grant (grant no.

EP/X029900/1), awarded through the European Research Council Starting Grant 2021 scheme. H. L. thanks the Department of Chemistry at the University of Oxford for a studentship. R. L. Z. H. and Y.-T. H. thank the Engineering and Physical Sciences Research Council (EPSRC, grant no. EP/V014498/2) for financial support. A. W. is supported by EPSRC project no. EP/X037754/1. R. L. Z. H. thanks the Royal Academy of Engineering through the Senior Research Fellowships scheme for financial support (grant no. RCSR2324-18-68).

Author contributions

R. L. Z. H. and A. W. conceived of the idea for this review and drafted the proposal, with support from the other authors. R. L. Z. H. wrote the introduction, Box 1 and Box 3, the definition of defect tolerance section, drafted the conclusions and outlook, and contributed to Fig. 1. I.M.-L. and A.W. wrote the models for defect tolerance in LHPs, prepared Box 2, and contributed to Fig. 1. J.Y. wrote the polaronic model sub-section in the main discussion and outlook section. H.L. prepared Fig. 3, and the discussion around that, while Y.-T.H. prepared Fig. 4 and the associated discussion. All authors edited and revised the manuscript together.

Competing interests

The authors declare no competing interests

Supplementary Information for

Multifaceted nature of defect tolerance in halide perovskites and emerging semiconductors

Irea Mosquera-Lois^{1,†}, Yi-Teng Huang^{2,†}, Hugh Lohan^{2,1,†}, Junzhi Ye², Aron Walsh^{1,*} and Robert L. Z. Hoye^{2,*}

¹ Department of Materials, Imperial College London, Exhibition Road, London SW1 2AZ, United Kingdom

² Inorganic Chemistry Laboratory, Department of Chemistry, University of Oxford, South Parks Road, Oxford OX1 3QR, United Kingdom

† These authors contributed equally

* e-mail: a.walsh@imperial.ac.uk (A.W.), robert.hoye@chem.ox.ac.uk (R. L. Z. H.)

Table S1 | Performance of lead-free perovskite-inspired materials in solar cells (1-sun illumination)

Year	Solar absorber	Device architecture	V_{oc} (V)	J_{sc} (mA cm ⁻²)	FF (%)	PCE (%)	Ref.
2015	FASnI ₃	FTO/c-TiO ₂ /mp-TiO ₂ /FASnI ₃ /Spiro-OMeTAD/Au	0.238	24.45	36	2.1	1
2016	FASnI ₃	FTO/c-TiO ₂ /mp-TiO ₂ /FASnI ₃ /Spiro-OMeTAD/Au	0.32	23.7	63	4.8	2
2016	FASnI ₃	FTO/c-TiO ₂ /mp-TiO ₂ /ZnS/FASnI ₃ /PTAA/Au	0.38	23.09	60.01	5.27	3
2017	FASnI ₃	FTO/c-TiO ₂ /mp-TiO ₂ /FASnI ₃ /PTAA/Au	0.48	22.54	64.47	7.14	4
2018	FASnI ₃	ITO/PEDOT:PSS/FASnI ₃ /BCP/Al	0.525	24.1	0.71	9	5
2019	FASnI ₃	FTO/NiO/FASnI ₃ /C ₆₀ /Au	0.97	25.95	80.85	9.99	6
2020	FASnI ₃	ITO/PEDOT:PSS/FASnI ₃ /C ₆₀ /BCP/Ag	0.638	21.95	72.5	10.16	7
2020	FASnI ₃	ITO/PEDOT:PSS/FASnI ₃ /PMMA/BCP/Ag	0.67	22.47	71.8	10.81	8
2020	FASnI ₃	ITO/PEDOT:PSS/FASnI ₃ /C ₆₀ /BCP/Ag	0.76	23.5	64	11.4	9
2021	FASnI ₃	ITO/PEDOT:PSS/FASnI ₃ /C ₆₀ /BCP/Ag	0.77	22.48	70	12.11	10
2021	FASnI ₃	ITO/PEDOT:PSS/FASnI ₃ /ICBA/BCP/Al	0.84	24.91	71	14.81	11
2024	FASnI ₃	ITO/PEDOT/FASnI ₃ /BCP/Ag	0.974	21.7	74.4	15.7	12
2017	MASnI ₃	FTO/c-TiO ₂ /mp-TiO ₂ /enMASnI ₃ :SnF ₂ /PTAA/Au	0.428 67	24.28	63.72	6.63	13
2019	MASnI ₃	FTO/c-TiO ₂ /mp-TiO ₂ /MASnI ₃ /PTAA/Au	0.426	22.91	64	7.13	14
2020	MASnI ₃	ITO/PEDOT:PSS/MASnI ₃ /PC ₆₁ BM/BCP/Ag	0.57	20.68	66	7.78	15
2022	MASnI ₃	ITO/PEDOT:PSS/MASnI ₃ -xEABr/PC ₆₁ BM/BCP/Ag	0.72	19.08	69.62	9.59	16
2024	MASnI ₃	ITO/PEDOT:PSS/MASnI ₃ /PC ₆₁ BM/BCP/Ag	0.74	22.3	62	10.2	17
2016	CsSnI ₃	ITO/TiO ₂ /m-TiO ₂ /CsSnI ₃ /Spiro-OMeTAD/Au	0.52	10.2	62.5	3.31	18
2016	CsSnI ₃	ITO/CsSnI ₃ /PC ₆₁ BM/BCP/Al	0.51	10.44	69	3.56	19
2017	CsSnI ₃	FTO/c-TiO ₂ /mp-TiO ₂ /CsSnI ₃ /PTAA:TPFB/Au	0.381	25.71	49.05	4.81	20
2019	CsSnI ₃	ITO/PEDOT:PSS/CsSnI ₃ /PCBM/Ag	-	-	-	5.03	21
2021	CsSnI ₃	FTO/c-TiO ₂ /mp-TiO ₂ /CsSnI ₃ -MBAA/P3HT/Au	0.45	24.85	67	7.5	22
2021	CsSnI ₃	ITO/PEDOT:PSS/CsSnI ₃ -PTM/ICBA/BCP/Ag	0.64	21.81	72.1	10.1	23
2022	CsSnI ₃	ITO/NiO _x /CsSnI ₃ /PCBM/ZrAcac/Ag	0.75	20.7	72.1	11.2	24
2023	CsSnI ₃	Ag/Spiro-OMeTAD/CsSnI ₃ /PCBM/Ag	0.78	25.13	59.8	11.7	25
2024	CsSnI ₃	ITO/PEDOT:PSS/CsSnI ₃ /3-ThMAI/ICBA/BCP/Ag	0.77	22.68	69	12.05	26
2016	MA ₃ Bi ₂ I ₉	ITO/PEDOT/MA ₃ Bi ₂ I ₉ /PCBM/Ca/Al	0.66	0.22	49	0.1	27
2016	MA ₃ Bi ₂ I ₉	ITO/c-TiO ₂ /mp-TiO ₂ /MA ₃ Bi ₂ I ₉ /Spiro-MeOTAD/MoO ₃ /Ag	0.67	1	62.48	0.42	28
2018	MA ₃ Bi ₂ I ₉	FTO/c-TiO ₂ /mp-TiO ₂ /MA ₃ Bi ₂ I ₉ /P3HT/Au	1.01	4.02	78	3.17	29
2015	Cs ₃ Bi ₂ I ₉	FTO/c-TiO ₂ /mp-TiO ₂ /Cs ₃ Bi ₂ I ₉ /Spiro-OMeTAD/Ag	0.85	2.15	60	1.09	30
2016	Cs ₃ Bi ₂ I ₉	FTO/c-TiO ₂ /mp-TiO ₂ /Cs ₃ Bi ₂ I ₉ /P3HT/Ag	0.26	0.18	37	0.02	31

2018	Cs ₃ Bi ₂ I ₉	FTO/mp-TiO ₂ /Cs ₃ Bi ₂ I ₉ /Spiro-OMeTAD/Au	0.49	0.67	63.6	0.21	32
2018	Cs ₃ Bi ₂ I ₉	FTO/TiO ₂ /Cs ₃ Bi ₂ I ₉ /CuI/Au	0.86	5.78	64.38	3.20	33
2019	Cs ₃ Bi ₂ I ₉	ITO/NiO _x /Cs ₃ Bi ₂ I ₉ /PCBM/Al:ZnO/Ag	0.74	3.42	51	1.26	34
2019	Cs ₃ Bi ₂ I ₉	ITO/NiO _x /Cs ₃ Bi ₂ I ₉ /PCBM/C ₆₀ /BCP/Ag	0.75	0.51	59	0.23	35
2019	Cs ₃ Bi ₂ I _{9-x} Br _x	ITO/NiO _x /Cs ₃ Bi ₂ I ₉ /PCBM/C ₆₀ /BCP/Ag	0.64	3.15	57	1.15	35
2020	Cs ₃ Bi ₂ I ₉	Al:ZnO/c-TiO ₂ /Cs ₃ Bi ₂ I ₉ /CuSCN/graphite	0.37	1.43	32	0.17	36
2020	Cs ₃ Bi ₂ I ₉	FTO/c-TiO ₂ /mp-TiO ₂ /Cs ₃ Bi ₂ I ₉ /PDBD-T/Au	0.86	0.25	35.27	0.08	37
2020	Cs ₃ Bi ₂ I ₉	FTO/TiO ₂ /Cs ₃ Bi ₂ I ₉ /CuI/Au	0.675	5.39	52	1.087	38
2022	Cs ₃ Bi ₂ I ₉	FTO/c-TiO ₂ /mp-TiO ₂ /Cs ₃ Bi ₂ I ₉ /C	1.01	3.60	77	2.81	39
2022	Cs ₃ Bi ₂ I ₉	FTO/c-TiO ₂ /mp-TiO ₂ /Cs ₃ Bi ₂ I ₉ /Spiro-OMeTAD/Au	0.50	3.58	54.42	0.98	40
2023	Cs ₃ Bi ₂ I ₉	FTO/TiO ₂ /Cs ₃ Bi ₂ I ₉ /CuI/Au	1.07	2.28	62.30	1.52	41
2022	Cs ₂ AgBiBr ₆	ITO/SnO ₂ /Cs ₂ AgBiBr ₆ /Spiro-OMeTAD/Au	0.92	11.4	60.93	6.37	42
2018	Cs ₃ Sb ₂ I ₉	FTO/c-TiO ₂ /mp-TiO ₂ /Cs ₃ Sb ₂ I ₉ /Spiro-OMeTAD/Au	0.404	0.13	58	0.03	43
2018	Cs ₃ Sb ₂ I ₉	ITO/PEDOT:PSS/Cs ₃ Sb ₂ I ₉ /PC ₇₀ BM/Al	0.72	5.31	38.97	1.49	44
2019	Cs ₃ Sb ₂ I ₉	FTO/c-TiO ₂ /Cs ₃ Sb ₂ I ₉ /Au	0.61	3.55	55.8	1.21	45
2020	Cs ₃ Sb ₂ I ₉	ITO/PEDOT:PSS/Cs ₃ Sb ₂ I ₉ /PC ₇₁ BM/Al	0.79	3.76	54	1.67	46
2020	Cs ₃ Sb ₂ I ₉	FTO/TiO ₂ /Cs ₃ Sb ₂ I ₉ /CuI/Au	0.653	4.56	46	1.036	47
2020	Cs ₃ Sb ₂ I _{9-x} Cl _x	ITO/PEDOT:PSS/Cs ₃ Sb ₂ I _{9-x} Cl _x /PC ₆₀ BM/Al	0.70	5.87	42	1.7	48
2021	Cs ₃ Sb ₂ I ₉	ITO/PEDOT:PSS/Cs ₃ Sb ₂ I ₉ /ITIC/PCBM/Ca/Ag	0.91	6.45	55	3.25	49
2022	Cs ₃ Sb ₂ I ₉	FTO/TiO ₂ /Cs ₃ Sb ₂ I ₉ /P3HT/Au	0.80	5.40	54.90	2.48	50
2022	Cs ₃ Sb ₂ I ₉	FTO/TiO ₂ /Cs ₃ Sb ₂ I ₉ /Spiro-OMeTAD/Au	0.622	3.69	47	1.07	51
2022	Cs ₃ Sb ₂ I _{9-x} Cl _x	FTO/Nb ₂ O ₅ /Cs ₃ Sb ₂ I _{9-x} Cl _x /P3HT/C	0.80	3.87	53	1.67	52
2022	Cs ₃ Sb ₂ I _{9-x} Cl _x	FTO/c-TiO ₂ /mp-TiO ₂ /Cs ₃ Sb ₂ I _{9-x} Cl _x /Spiro-OMeTAD/Au	0.65	6.77	50.3	2.22	53
2022	Cs ₃ Sb ₂ I _{9-x} Cl _x	ITO/PEDOT:PSS/Cs ₃ Sb ₂ I _{9-x} Cl _x /PMMA/PCBM/Al	0.87	6.55	50	2.85	54
2023	Cs ₃ Sb ₂ I ₉	FTO/c-TiO ₂ /Cs ₃ Sb ₂ I ₉ /Au	0.62	5.57	51.4	1.76	55
2023	Cs ₃ Sb ₂ I _{9-x} Cl _x	FTO/a-Nb ₂ O ₅ /Cs ₃ Sb ₂ I _{9-x} Cl _x /P3HT/C	0.83	4.04	52	1.75	56
2023	Cs ₃ Sb ₂ I _{9-x} Cl _x	FTO/TiO ₂ /Cs ₃ Sb ₂ I _{9-x} Cl _x /Spiro-OMeTAD/Au	0.84	7.13	54.2	3.2	57
2013	AgBiS ₂	FTO/c-TiO ₂ /mp-TiO ₂ /AgBiS ₂ /(Na ₂ S+S+KCl+NaOH)/Au	0.18	7.61	38.6	0.53	58
2015	AgBiS ₂	FTO/TiO ₂ NRs/AgBiS ₂ /(LiI+I ₂ +DMPPII+4-TPB)/Pt-coated FTO	0.53	4.22	43	0.95	59
2016	AgBiS ₂	ITO/ZnO/AgBiS ₂ /PTB7/MoO ₃ /Ag	0.45	22.1	65	6.3	60
2018	AgBiS ₂	ITO/ZnO/AgBiS ₂ /P3HT/Au	0.46	16.7	56	4.3	61
2018	AgBiS ₂	ITO/ZnO/AgBiS ₂ /Spiro-OMeTAD/MoO ₃ /Ag	0.241	18.1	35	1.5	62
2019	AgBiS ₂	FTO/TiO ₂ /AgBiS ₂ /Co:P3HT/C/Ag	0.50	13.27	43	2.87	63
2019	AgBiS ₂	FTO/ZnO/AgBiS ₂ /P3HT/MoO ₃ /Al	0.23	16.56	36.75	1.40	64
2019	AgBiS ₂	ITO/ZnO/AgBiS ₂ /PTB7/MoO ₃ /Ag	0.51	17.63	64	5.75	65
2020	AgBiS ₂	ITO/ZnO/AgBiS ₂ /PTB7/MoO ₃ /Ag	0.46	22.68	61	6.37	66
2020	AgBiS ₂	ITO/ZnO/AgBiS ₂ /P3HT/MoO ₃ /Au	0.41	15.06	54	3.31	67
2020	AgBiS ₂	ITO/PEDOT:PSS/AgBiS ₂ /BCP/C ₆₀ /Cu	0.28	16.85	43.3	2.04	68
2020	AgBiS ₂	FTO/ZnO/AgBiS ₂ /PTB7-Th/MoO ₃ /Ag	0.445	18.87	54.4	4.57	69
2020	AgBiS ₂	ITO/ZnO/AgBiS ₂ /PTB7/MoO ₃ /Ag	0.43	22.07	59	5.55	70

2020	AgBiS ₂	ITO/ZnO/AgBiS ₂ /PTB7/MoO ₃ /Ag	0.55	12.41	59	4.08	71
2021	AgBiS ₂	ITO/ZnO NWs/AgBiS ₂ /P3HT/Au	0.378	20.54	55.3	4.14	72
2021	AgBiS ₂	ITO/NiO/AgBiS ₂ /ZnO/Al	0.50	18.54	61	5.59	73
2021	AgBiS ₂	ITO/NiO/AgBiS ₂ /PCBM/BCP/Ag	0.38	20.71	54	4.25	74
2022	AgBiS ₂	FTO/c-TiO ₂ /mp-TiO ₂ / AgBiS ₂ /Spiro-OMeTAD:P3HT	0.35	4.59	56.47	0.91	75
2022	AgBiS ₂	ITO/ZnO/AgBiS ₂ /P3HT/Au	0.436	12.64	56.7	3.12	76
2022	AgBiS ₂	ITO/ZnO/AgBiS ₂ / PBDB-T-2F/MoO ₃ /Ag	0.494	27.07	68.1	9.10	77
2022	AgBiS ₂	ITO/SnO ₂ /AgBiS ₂ /PTAA/MoO ₃ /Ag	0.495	27.11	68	9.17	78
2022	AgBiS ₂	FTO/TiO ₂ /AgBiS ₂ /NiO/CuS	0.24	30.2	29.8	2.1	79
2022	AgBiS ₂	ITO/SnO ₂ /AgBiS ₂ /PTAA/MoO ₃ /Ag	0.48	24.9	61	7.3	80
2022	AgBiS ₂	ITO/ZnO-NWs/AgBiS ₂ /P3HT/Au	0.41	22.21	60	5.41	81
2022	AgBiS ₂	ITO/SnO ₂ /AgBiS ₂ /PTB7/MoO ₃ /Ag	0.48	23.97	64	7.33	82
2022	AgBiS ₂	FTO/TiO ₂ /AgBiS ₂ /NiO/CuS	0.30	16.1	49.7	2.0	83
2023	AgBiS ₂	FTO/c-TiO ₂ /mp-TiO ₂ /AgBiS ₂ / (N719+I ₂)/Pt	0.78	14.87	72	8.36	84
2024	AgBiS ₂	SLG/Mo/AgBiS ₂ /CdS/ITO/Ag	0.096 5	4.68	26	0.13	85
2024	AgBiS ₂	FTO/SnO ₂ /AgBiS ₂ /Spiro- OMeTAD/Au	0.28	30.9	41.9	3.68	86
2024	AgBiS ₂	ITO/SnO ₂ /AgBiS ₂ /PTAA/MoO ₃ /Ag	0.486	23.81	64	7.35	87
2024	AgBiS ₂	ITO/ZnO/AgBiS ₂ /PTB7/MoO ₃ /Ag	0.54	22.6	67.44	8.14	88
2024	AgBiS ₂	ITO/SnO ₂ /AgBiS ₂ /PTAA/MoO ₃ /Au	0.518	27.20	72.4	10.20	89
2020	BiI ₃	ITO/PEDOT/BiI ₃ +PCBM/BCP/Ag	0.47	8.76	36.5	1.50	90
2010	BiOI	FTO/TiO ₂ /BiOI/electrolyte/Pt/FTO	0.62	0.24	61	0.092	91
2015	BiOI	FTO/TiO ₂ /BiOI/electrolyte/Pt/FTO	0.61	3.8	45	1.03	92
2017	BiOI	ITO/NiO _x /BiOI/ZnO/Al	0.75	7.0	43	1.82	93
2019	SbSI	FTO/c-TiO ₂ /mp- TiO ₂ /SbSI/PCPDTBT/Au	0.60	9.62	65.2	3.62	94
2014	CuSbS ₂	Mo/CuSbS ₂ /CdS/Al:ZnO	0.49	14.73	44	3.13	95
2016	CuSbS ₂	Mo/CuSbS ₂ /CdS/i-ZnO/n-ZnO/Al	0.47	15.6	43.6	3.22	96
2015	CuSbSe ₂	FTO/CuSbSe ₂ /CdS/ZnO/ITO/Al	0.274	11.84	40.51	1.32	97
2015	CuSbSe ₂	Mo/CuSbSe ₂ /CdS/i- ZnO/ZnO/Ni:Al/MgF	0.35	22.82	-	3.5	98
2017	CuSbSe ₂	Mo/CuSbSe ₂ /CdS/i- ZnO/ZnO/Ni:Al/MgF	0.336	26	53	4.7	99
2014	Sb ₂ Se ₃	FTO/c-TiO ₂ /m-TiO ₂ /Sb ₂ Se ₃ /PEDOT:PSS/Au	0.304 5	22.3	47.2	3.21	100
2014	Sb ₂ Se ₃	FTO/CdS/Sb ₂ Se ₃ /Au	0.335	24.4	46.8	3.7	101
2015	Sb ₂ Se ₃	ITO/CdS/Sb ₂ Se ₃ /Au	0.36	25.3	52.5	4.8	102
2015	Sb ₂ Se ₃	FTO/CdS/Sb ₂ Se ₃ /Au	0.4	25.1	55.7	5.6	103
2017	Sb ₂ Se ₃	TiO ₂ /CdS/GQDs-C-fabric/NiO/ Sb ₂ Se ₃	0.63	25.49	45	7.19	104
2019	Sb ₂ Se ₃	ZnO:Al/ZnO/CdS/TiO ₂ /Sb ₂ Se ₃ - NRs/MoSe ₂ /Mo	0.4	32.58	70.3	9.2	105
2022	Sb ₂ Se ₃	Mo/MoSe ₂ /Sb ₂ Se ₃ /CdS/ZnO/AZO	0.488	30.86	67.17	10.12	106
2022	Sb ₂ Se ₃	FTO/CdS/Sb ₂ Se ₃ /Spiro- OMeTAD/Au	0.767	33.52	67.64	10.57	107
2009	Sb ₂ S ₃	FTO/TiO ₂ /Sb ₂ S ₃ /CuSCN/Au	0.49	14.1	48.8	3.37	108
2010	Sb ₂ S ₃	FTO/TiO ₂ / Sb ₂ S ₃ /(LiSCN)CuSCN/Au	0.56	11.6	58	3.7	109
2010	Sb ₂ S ₃	FTO/TiO ₂ /Sb ₂ S ₃ /Spiro/Au	0.556	12.3	69.9	5.06	110
2011	Sb ₂ S ₃	FTO/TiO ₂ / Sb ₂ S ₃ /PCDTBT/PTAA/Au	0.616	15.3	65.7	6.18	111
2012	Sb ₂ S ₃	FTO/TiO ₂ /Sb ₂ S ₃ /P3HT/PCBM/Au	0.595	16	65.5	6.3	112
2014	Sb ₂ S ₃	FTO/mp- TiO ₂ /Sb ₂ S ₃ /PCPDTBT/PEDOT:PS S/Au	0.711	16.1	65	7.5	113
2015	Sb ₂ S ₃	FTO/TiO ₂ /Sb ₂ S ₃ /P3HT/PEDOT:PS S/Au	0.595	16.1	66.5	6.4	114
2018	Sb ₂ S ₃	FTO/TiO ₂ /Sb ₂ S ₃ /Spiro- OMeTAD/Au	0.671	18.43	54.8	6.78	115

2020	Sb ₂ S ₃	FTO/TiO ₂ / Sb ₂ S ₃ /PCPDTBT/PEDOT:PSS/Au	0.521	21.5	63	7.05	116
2020	Sb ₂ S ₃	FTO/TiO ₂ /SbCl ₃ -treated Sb ₂ S ₃ /Spiro-OMeTAD/Au	0.72	17.24	57.18	7.1	117
2022	Sb ₂ S ₃	FTO/CdS/Sb ₂ S ₃ /Spiro- OMeTAD/Au	0.757	17.41	60.48	8	118
2023	Sb ₂ S ₃	FTO/SnO ₂ /CdS/Sb ₂ S ₃ /Spiro- OMeTAD/Au	0.796	16.7	57.7	7.66	119
2023	Sb ₂ S ₃	ITO/TiO ₂ /CdS/Sb ₂ S ₃ / Spiro- OMeTAD/MoO ₃ /Ag	0.75	17.18	60	7.73	120
2009	Sb ₂ (S _x Se _{1-x}) ₃	d-SnO ₂ /CdS/ Sb ₂ (S _x Se _{1-x}) ₃ :Sb ₂ O ₃ /PbS	0.52	4.2	28	0.66	121
2014	Sb ₂ (S _x Se _{1-x}) ₃	FTO/c-TiO ₂ /mp- TiO ₂ /Sb ₂ S ₃ /Sb ₂ Se ₃ /P3HT/Au	0.474 8	24.9	55.6	6.6	122
2019	Sb ₂ (S _x Se _{1-x}) ₃	FTO/TiO ₂ /CdS:In/ Sb ₂ (S _x Se _{1-x}) ₃ /Spiro-OMeTAD/Au	0.59	18.1	62	6.63	123
2020	Sb ₂ (S _x Se _{1-x}) ₃	FTO/CdS/Sb ₂ (S _x Se _{1-x}) ₃ /Spiro- OMeTAD/ Au	0.63	23.7	68	10	124
2020	Sb ₂ (S _x Se _{1-x}) ₃	FTO/CdS/Sb ₂ (S _x Se _{1-x}) ₃ /Spiro- OMeTAD/Au	0.664	23.8	66	10.5	125
2022	Sb ₂ (S _x Se _{1-x}) ₃	FTO/Zn(O,S)/CdS/ Sb ₂ (S _x Se _{1-x}) ₃ /Spiro-OMeTAD/Au	0.673	23.7	67	10.7	126
2023	Sb ₂ (S _x Se _{1-x}) ₃	glass/FTO/CdS/ Sb ₂ (S _x Se _{1-x}) ₃ /Spiro-OMeTAD/Au	0.63	25.27	67.35	10.75	127

Abbreviations - mesoporous TiO₂ (mp-TiO₂), compact TiO₂ (c-TiO₂), Graphene Quantum Dots (GQDs), Al₂O₃:ZnO (AZO), Nanorods (NRs), doped SnO₂ (d-SnO₂), phthalimide (PTM), 3-thiophenemethylammonium iodide (3-ThMAI), indene-C₆₀ bisadduct (ICBA), bahocuproine (BCP), (Spiro-OMeTAD), Poly[2,6-(4,4-bis(2-ethylhexyl)-4*H*-cyclopenta[2,1-b;3,4-b']dithiophene)-*alt*-4,7(2,1,3-benzothiadiazole)] (PCPDTBT), Poly(3,4-ethylenedioxythiophene) polystyrene sulfonate (PEDOT:PSS), Poly[bis(4-phenyl)(2,4,6-trimethylphenyl)amine (PTAA), Poly({4,8-bis[(2-ethylhexyl)oxy]benzo[1,2-b:4,5-b']dithiophene-2,6-diyl}{3-fluoro-2-[(2-ethylhexyl)carbonyl]thieno[3,4-b]thiophenediyl}) (PTB7), [6,6]-Phenyl C61 butyric acid methyl ester (PCBM), Poly[(2,6-(4,8-bis(5-(2-ethylhexyl)thiophen-2-yl)-benzo[1,2-b:4,5-b']dithiophene))-*alt*-(5,5-(1',3'-di-2-thienyl-5',7'-bis(2-ethylhexyl)benzo[1',2'-c:4',5'-c']dithiophene-4,8-dione)] (PDBD-T), N,N'-methylenebis(acrylamide) (MBAA), ethylammonium bromide (EABr), Poly[[4,8-bis[5-(2-ethylhexyl)-4-fluoro-2-thienyl]benzo[1,2-b:4,5-b']dithiophene-2,6-diyl]-2,5-thiophenediyl[5,7-bis(2-ethylhexyl)-4,8-dioxo-4*H*,8*H*-benzo[1,2-c:4,5-c']dithiophene-1,3-diyl]-2,5-thiophenediyl] (PDBD-T-2F)

Reference

1. Koh, T. M. *et al.* Formamidinium tin-based perovskite with low *E_g* for photovoltaic applications. *J Mater Chem A* **3**, 14996–15000 (2015).
2. Lee, S. J. *et al.* Fabrication of Efficient Formamidinium Tin Iodide Perovskite Solar Cells through SnF₂–Pyrazine Complex. *J Am Chem Soc* **138**, 3974–3977 (2016).
3. Ke, W. *et al.* TiO₂–ZnS Cascade Electron Transport Layer for Efficient Formamidinium Tin Iodide Perovskite Solar Cells. *J Am Chem Soc* **138**, 14998–15003 (2016).
4. Ke, W. *et al.* Enhanced photovoltaic performance and stability with a new type of hollow 3D perovskite {en}FASnI₃. *Sci Adv* **3**, e1701293 (2024).
5. Shao, S. *et al.* Highly Reproducible Sn-Based Hybrid Perovskite Solar Cells with 9% Efficiency. *Adv Energy Mater* **8**, 1702019 (2018).

6. Dixit, H., Punetha, D. & Pandey, S. K. Improvement in performance of lead free inverted perovskite solar cell by optimization of solar parameters. *Optik (Stuttg)* **179**, 969–976 (2019).
7. Meng, X. *et al.* Surface-Controlled Oriented Growth of FASnI₃ Crystals for Efficient Lead-free Perovskite Solar Cells. *Joule* **4**, 902–912 (2020).
8. Yin, Y., Wang, M., Malgras, V. & Yamauchi, Y. Stable and Efficient Tin-Based Perovskite Solar Cell via Semiconducting–Insulating Structure. *ACS Appl Energy Mater* **3**, 10447–10452 (2020).
9. Wang, C. *et al.* Self-Repairing Tin-Based Perovskite Solar Cells with a Breakthrough Efficiency Over 11%. *Advanced Materials* **32**, 1907623 (2020).
10. Cui, D. *et al.* Making Room for Growing Oriented FASnI₃ with Large Grains via Cold Precursor Solution. *Adv Funct Mater* **31**, 2100931 (2021).
11. Yu, B.-B. *et al.* Heterogeneous 2D/3D Tin-Halides Perovskite Solar Cells with Certified Conversion Efficiency Breaking 14%. *Advanced Materials* **33**, 2102055 (2021).
12. Shi, Y., Zhu, Z., Miao, D., Ding, Y. & Mi, Q. Interfacial Dipoles Boost Open-Circuit Voltage of Tin Halide Perovskite Solar Cells. *ACS Energy Lett* **9**, 1895–1897 (2024).
13. Ke, W. *et al.* Efficient Lead-Free Solar Cells Based on Hollow {en}MASnI₃ Perovskites. *J Am Chem Soc* **139**, 14800–14806 (2017).
14. Li, F. *et al.* A Cation-Exchange Approach for the Fabrication of Efficient Methylammonium Tin Iodide Perovskite Solar Cells. *Angewandte Chemie International Edition* **58**, 6688–6692 (2019).
15. Wang, P. *et al.* Ion Exchange/Insertion Reactions for Fabrication of Efficient Methylammonium Tin Iodide Perovskite Solar Cells. *Advanced Science* **7**, 1–7 (2020).
16. Ji, L. *et al.* Regulating crystallization dynamics and crystal orientation of methylammonium tin iodide enables high-efficiency lead-free perovskite solar cells. *Nanoscale* **14**, 1219–1225 (2022).
17. Xu, F., Wei, H. & Cao, B. A hot phonon bottleneck observed upon incorporation of SnF₂ to MASnI₃ films and its possible role in increasing photocarrier diffusion length. *J Appl Phys* **135**, 133102 (2024).
18. Wang, N. *et al.* Heterojunction-Depleted Lead-Free Perovskite Solar Cells with Coarse-Grained B-γ-CsSnI₃ Thin Films. *Adv Energy Mater* **6**, 1601130 (2016).
19. Marshall, K. P., Walker, M., Walton, R. I. & Hatton, R. A. Enhanced stability and efficiency in hole-transport-layer-free CsSnI₃ perovskite photovoltaics. *Nat Energy* **1**, 16178 (2016).
20. Song, T.-B., Yokoyama, T., Aramaki, S. & Kanatzidis, M. G. Performance Enhancement of Lead-Free Tin-Based Perovskite Solar Cells with Reducing Atmosphere-Assisted Dispersible Additive. *ACS Energy Lett* **2**, 897–903 (2017).
21. Wang, Y. *et al.* Convenient preparation of CsSnI₃ quantum dots, excellent stability, and the highest performance of lead-free inorganic perovskite solar cells so far. *J Mater Chem A* **7**, 7683–7690 (2019).

22. Ye, T. *et al.* Ambient-Air-Stable Lead-Free CsSnI₃ Solar Cells with Greater than 7.5% Efficiency. *J Am Chem Soc* **143**, 4319–4328 (2021).
23. Ye, T. *et al.* Localized Electron Density Engineering for Stabilized B-γ CsSnI₃-Based Perovskite Solar Cells with Efficiencies >10%. *ACS Energy Lett* **6**, 1480–1489 (2021).
24. Zhang, W. *et al.* Organic-Free and Lead-Free Perovskite Solar Cells with Efficiency over 11%. *Adv Energy Mater* **12**, 2202491 (2022).
25. Dai, L. *et al.* Single-Crystal Nanowire Cesium Tin Triiodide Perovskite Solar Cell. *Small* **19**, 2208062 (2023).
26. Zhang, Z. *et al.* Over 12% efficient CsSnI₃ perovskite solar cells enabled by surface post-treatment with bi-functional polar molecules. *Chemical Engineering Journal* **490**, 151561 (2024).
27. Öz, S. *et al.* Zero-dimensional (CH₃NH₃)₃Bi₂I₉ perovskite for optoelectronic applications. *Solar Energy Materials and Solar Cells* **158**, 195–201 (2016).
28. Zhang, X. *et al.* Active-layer evolution and efficiency improvement of (CH₃NH₃)₃Bi₂I₉-based solar cell on TiO₂-deposited ITO substrate. *Nano Res* **9**, 2921–2930 (2016).
29. Jain, S. M. *et al.* An effective approach of vapour assisted morphological tailoring for reducing metal defect sites in lead-free, (CH₃NH₃)₃Bi₂I₉ bismuth-based perovskite solar cells for improved performance and long-term stability. *Nano Energy* **49**, 614–624 (2018).
30. Park, B. W. *et al.* Bismuth Based Hybrid Perovskites A₃Bi₂I₉ (A: Methylammonium or Cesium) for Solar Cell Application. *Advanced Materials* **27**, 6806–6813 (2015).
31. Johansson, M. B., Zhu, H. & Johansson, E. M. J. Extended Photo-Conversion Spectrum in Low-Toxic Bismuth Halide Perovskite Solar Cells. *Journal of Physical Chemistry Letters* **7**, 3467–3471 (2016).
32. Ghosh, B. *et al.* Limitations of Cs₃Bi₂I₉ as Lead-Free Photovoltaic Absorber Materials. *ACS Appl Mater Interfaces* **10**, 35000–35007 (2018).
33. Bai, F. *et al.* Lead-free, air-stable ultrathin Cs₃Bi₂I₉ perovskite nanosheets for solar cells. *Solar Energy Materials and Solar Cells* **184**, 15–21 (2018).
34. Khadka, D. B., Shirai, Y., Yanagida, M. & Miyano, K. Tailoring the film morphology and interface band offset of caesium bismuth iodide-based Pb-free perovskite solar cells. *J Mater Chem C* **7**, 8335–8343 (2019).
35. Yu, B. Bin *et al.* Alloy-induced phase transition and enhanced photovoltaic performance: The case of Cs₃Bi₂I_{9-x}Br_x perovskite solar cells. *J Mater Chem A* **7**, 8818–8825 (2019).
36. Waykar, R. *et al.* Environmentally stable lead-free cesium bismuth iodide (Cs₃Bi₂I₉) perovskite: Synthesis to solar cell application. *Journal of Physics and Chemistry of Solids* **146**, 109608 (2020).
37. Hu, W. *et al.* Bulk heterojunction gifts bismuth-based lead-free perovskite solar cells with record efficiency. *Nano Energy* **68**, 104362 (2020).

38. Ahmad, K., Kumar, P. & Mobin, S. M. Inorganic Pb-Free Perovskite Light Absorbers for Efficient Perovskite Solar Cells with Enhanced Performance. *Chem Asian J* **15**, 2859–2863 (2020).
39. Photodetector, M. L. P. *et al.* Potassium Iodide-Modified Lead-Free Cs₃Bi₂I₉ Perovskites for Enhanced High-Efficiency Solar Cells. *Nanomaterials* **12**, 3751 (2022).
40. Masawa, S. M., Li, J., Zhao, C., Liu, X. & Yao, J. 0D/2D Mixed Dimensional Lead-Free Caesium Bismuth Iodide Perovskite for Solar Cell Application. *Materials* **15**, (2022).
41. Yuan, W. *et al.* Environmental lead-free Cs₃Bi₂I₉ films deposited by vapor transport deposition for stable all-inorganic solar cells. *Opt Mater (Amst)* **139**, (2023).
42. Zhang, Z. *et al.* Hydrogenated Cs₂AgBiBr₆ for significantly improved efficiency of lead-free inorganic double perovskite solar cell. *Nat Commun* **13**, 1–12 (2022).
43. Correa-Baena, J.-P. P. *et al.* A-Site Cation in Inorganic A₃Sb₂I₉ Perovskite Influences Structural Dimensionality, Exciton Binding Energy, and Solar Cell Performance. *Chemistry of Materials* **30**, 3734–3742 (2018).
44. Singh, A. *et al.* Photovoltaic Performance of Vapor-Assisted Solution-Processed Layer Polymorph of Cs₃Sb₂I₉. *ACS Appl Mater Interfaces* **10**, 2566–2573 (2018).
45. Farooq, U. *et al.* Surface Defects Passivation with Organic Salt for Highly Stable and Efficient Lead-Free Cs₃Sb₂I₉ Perovskite Solar Cells. *ACS Appl Energy Mater* **6**, 10294–10302 (2023).
46. Singh, A. *et al.* Modulating Performance and Stability of Inorganic Lead-Free Perovskite Solar Cells via Lewis-Pair Mediation. *ACS Appl Mater Interfaces* **12**, 32649–32657 (2020).
47. Ahmad, K., Kumar, P. & Mobin, S. M. Inorganic Pb-Free Perovskite Light Absorbers for Efficient Perovskite Solar Cells with Enhanced Performance. *Chem Asian J* **15**, 2859–2863 (2020).
48. Paul, G., Pal, A. J. & Larson, B. W. Structure, Morphology, and Photovoltaic Implications of Halide Alloying in Lead-Free Cs₃Sb₂Cl_xI_{9-x} 2D-Layered Perovskites. *Solar RRL* **5**, 1–8 (2021).
49. Singh, A. *et al.* Panchromatic heterojunction solar cells for Pb-free all-inorganic antimony based perovskite. *Chemical Engineering Journal* **419**, 129424 (2021).
50. Hiltunen, A., Lamminen, N., Salonen, H., Liu, M. & Vivo, P. Efficiency improvement for perovskite-inspired Cs₃Sb₂I₉ solar cells using P3HT as the hole transport material. *Sustain Energy Fuels* **6**, 217–222 (2022).
51. Ahmad, K., Khan, M. Q. & Kim, H. Simulation and fabrication of all-inorganic antimony halide perovskite-like material based Pb-free perovskite solar cells. *Opt Mater (Amst)* **128**, 112374 (2022).
52. Zhao, F. *et al.* Enhancing photovoltaic performance of carbon-based planar Cs₃Sb₂I_{9-x}Cl_x solar cells by using P3HT as hole transport material. *J Alloys Compd* **897**, 162741 (2022).

53. Li, J., Lv, Y., Han, H., Xu, J. & Yao, J. Two-Dimensional Cs₃Sb₂I_{9-x}Cl_x Film with (201) Preferred Orientation for Efficient Perovskite Solar Cells. *Materials* **15**, 1–13 (2022).
54. Paul, G. & Pal, A. J. Impact of band-engineered polymer-interlayers on heterojunction solar cells based on 2D-layered perovskites (Cs₃Sb₂Cl_xI_{9-x}). *Solar Energy* **232**, 196–203 (2022).
55. Farooq, U. *et al.* Surface Defects Passivation with Organic Salt for Highly Stable and Efficient Lead-Free Cs₃Sb₂I₉ Perovskite Solar Cells. *ACS Appl Energy Mater* **6**, 10294–10302 (2023).
56. Zhao, F., Yang, P. & Chu, J. Differential impact of a-Nb₂O₅ and a-TiO₂ ETL on the photoelectric performance of Cs₃Sb₂I_{9-x}Cl_x perovskite solar cells. *Journal of Optoelectronics and Advanced Materials* **25**, 326–333 (2023).
57. Zhang, Y. *et al.* Controlling the Intermediate Phase to Improve the Crystallinity and Orientation of Cs₃Sb₂Cl_xI_{9-x} Films for Efficient Solar Cells. *Adv Funct Mater* **33**, 1–8 (2023).
58. Huang, P., Yang, W. & Lee, M. AgBiS₂ Semiconductor-Sensitized Solar Cells. *J Phys Chem* **117**, 18308–18314 (2013).
59. Zhou, S. *et al.* Preparation and Photovoltaic Properties of Ternary AgBiS₂ Quantum Dots Sensitized TiO₂ Nanorods Photoanodes by Electrochemical Atomic Layer Deposition. *J Electrochem Soc* **163**, D63–D67 (2016).
60. Bernechea, M. M. *et al.* Solution-processed solar cells based on environmentally friendly AgBiS₂ nanocrystals. *Nat Photonics* **10**, 521–525 (2016).
61. Hu, L. *et al.* Enhanced optoelectronic performance in AgBiS₂ nanocrystals obtained via an improved amine-based synthesis route. *J Mater Chem C Mater* **6**, 731–737 (2018).
62. Pai, N. *et al.* Spray deposition of AgBiS₂ and Cu₃BiS₃ thin films for photovoltaic applications. *J Mater Chem C* **6**, 2483–2494 (2018).
63. Calva-Yáñez, J. C. *et al.* Interfacial evolution of AgBiS₂ absorber layer obtained by SILAR method in hybrid solar cells. *J Phys D Appl Phys* **52**, (2019).
64. Wu, Y., Wan, L., Zhang, W., Li, X. & Fang, J. In situ grown silver bismuth sulfide nanorod arrays and their application to solar cells. *CrystEngComm* **21**, 3137–3141 (2019).
65. Oh, J. T. *et al.* Water-resistant AgBiS₂ colloidal nanocrystal solids for eco-friendly thin film photovoltaics. *Nanoscale* **11**, 9633–9640 (2019).
66. Burgués-Ceballos, I., Wang, Y., Akgul, M. Z. & Konstantatos, G. Colloidal AgBiS₂ nanocrystals with reduced recombination yield 6.4% power conversion efficiency in solution-processed solar cells. *Nano Energy* **75**, (2020).
67. Öberg, V. A., Johansson, M. B., Zhang, X. & Johansson, E. M. J. Cubic AgBiS₂ Colloidal Nanocrystals for Solar Cells. *ACS Appl Nano Mater* **3**, 4014–4024 (2020).
68. Jiang, L. *et al.* Solution-processed AgBiS₂ photodetectors from molecular precursors. *J Mater Chem C Mater* **8**, 2436–2441 (2020).
69. Ming, S. *et al.* Eco-friendly and stable silver bismuth disulphide quantum dot solar cells via methyl acetate purification and modified ligand exchange. *J Clean Prod* **246**, (2020).

70. Akgul, M. Z., Figueroba, A., Pradhan, S., Bi, Y. & Konstantatos, G. Low-Cost RoHS Compliant Solution Processed Photovoltaics Enabled by Ambient Condition Synthesis of AgBiS₂ Nanocrystals. *ACS Photonics* **7**, 588–595 (2020).
71. Bae, S. Y. *et al.* Improved Eco-Friendly Photovoltaics Based on Stabilized AgBiS₂ Nanocrystal Inks. *Chemistry of Materials* **32**, 10007–10014 (2020).
72. Xiao, Y. *et al.* Eco-friendly AgBiS₂ nanocrystal/ZnO nanowire heterojunction solar cells with enhanced carrier collection efficiency. *ACS Appl Mater Interfaces* **13**, 3969–3978 (2021).
73. Oh, J. T. *et al.* Ultra-stable all-inorganic silver bismuth sulfide colloidal nanocrystal photovoltaics using pin type architecture. *J Power Sources* **514**, 230585 (2021).
74. Chen, D. *et al.* Solution-Processed, Inverted AgBiS₂ Nanocrystal Solar Cells. *ACS Appl Mater Interfaces* **14**, 1634–1642 (2022).
75. Tang, F., Yao, X., Ying, C., Xu, L. & Shi, C. The Preparation of AgBiS₂ Sensitized TiO₂ Nanorod Array Solar Cells and Photovoltaic Performance of the Corresponding Solar Cells. *Chem Lett* **51**, 577–580 (2022).
76. Xiao, Y. *et al.* Halide-ligand-dependent Performance of AgBiS₂ Nanocrystal/ZnO Heterojunction Solar Cells. *Chem Lett* **51**, 1004–1007 (2022).
77. Kim, C., Kozakci, I., Kim, J., Lee, S. Y. & Lee, J. Y. Highly Efficient (>9%) Lead-Free AgBiS₂ Colloidal Nanocrystal/Organic Hybrid Solar Cells. *Adv Energy Mater* **12**, 2–9 (2022).
78. Wang, Y. *et al.* Cation disorder engineering yields AgBiS₂ nanocrystals with enhanced optical absorption for efficient ultrathin solar cells. *Nat Photonics* **16**, 235–241 (2022).
79. Akhil, S., Kusuma, J. & Balakrishna, R. G. Green AgBiSe₂/AgBiS₂ core shell quantum dots for stable solar cells by robust SILAR method. *J Clean Prod* **366**, 132760 (2022).
80. Wang, Y., Peng, L., Wang, Z. & Konstantatos, G. Environmentally Friendly AgBiS₂ Nanocrystal Inks for Efficient Solar Cells Employing Green Solvent Processing. *Adv Energy Mater* **12**, 1–7 (2022).
81. Xiao, Y. *et al.* Emission Spectroscopy Investigation of the Enhancement of Carrier Collection Efficiency in AgBiS₂-Nanocrystal/ZnO-Nanowire Heterojunction Solar Cells. *ACS Appl Mater Interfaces* **14**, 6994–7003 (2022).
82. Burgués-Ceballos, I., Wang, Y. & Konstantatos, G. Mixed AgBiS₂ nanocrystals for photovoltaics and photodetectors. *Nanoscale* **14**, 4987–4993 (2022).
83. Akhil, S. *et al.* Manifestation of the Enhanced Photovoltaic Performance in Eco-Friendly AgBiS₂ Solar Cells Using Titanium Oxynitride as the Electron Transport Layer. *Energy and Fuels* **36**, 14393–14402 (2022).
84. Zhang, J., Chen, X., Dong, L. & Zheng, W. The Photovoltaic Performance of Inorganic Quantum Dots and Organometallic Dye Co-sensitized Solar Cells. *J Inorg Organomet Polym Mater* **33**, 2531–2536 (2023).
85. Chalapathi, U. *et al.* Synthesis of AgBiS₂ films by sulfurizing Bi/Ag stacks for thin film photovoltaics. *Opt Mater (Amst)* **152**, 115492 (2024).

86. Li, Z. *et al.* Precisely tailoring the precursor solution for efficient AgBiS₂ solar cells. *CrystEngComm* **26**, 3026–3032 (2024).
87. Senina, A., Prudnikau, A., Wrzesińska-Lashkova, A., Vaynzof, Y. & Paulus, F. Cation exchange synthesis of AgBiS₂ quantum dots for highly efficient solar cells. *Nanoscale* **16**, 9325–9334 (2024).
88. Kim, D. *et al.* Multi-Facet Passivation of Ternary Colloidal Quantum Dot Enabled by Quadruple-Ligand Ensemble toward Efficient Lead-Free Optoelectronics. *Adv Energy Mater* **14**, 1–10 (2024).
89. Li, X. *et al.* Thin film AgBiS₂ solar cells with over 10 % power conversion efficiency enabled by vapor-assisted solution process treatment. *Chemical Engineering Journal* **495**, 153328 (2024).
90. Kang, J. *et al.* An inverted BiI₃/PCBM binary quasi-bulk heterojunction solar cell with a power conversion efficiency of 1.50%. *Nano Energy* **73**, 104799 (2020).
91. Wang, K., Jia, F., Zheng, Z. & Zhang, L. Crossed BiOI flake array solar cells. *Electrochem commun* **12**, 1764–1767 (2010).
92. Sfaelou, S., Raptis, D., Dracopoulos, V. & Lianos, P. BiOI solar cells. *RSC Adv* **5**, 95813–95816 (2015).
93. Hoye, R. L. Z. *et al.* Strongly Enhanced Photovoltaic Performance and Defect Physics of Air-Stable Bismuth Oxyiodide (BiOI). *Advanced Materials* **29**, 1702176 (2017).
94. Nie, R. & Seok, S. II. Efficient Antimony-Based Solar Cells by Enhanced Charge Transfer. *Small Methods* **4**, 1900698 (2020).
95. Septina, W., Ikeda, S., Iga, Y., Harada, T. & Matsumura, M. Thin film solar cell based on CuSbS₂ absorber fabricated from an electrochemically deposited metal stack. *Thin Solid Films* **550**, 700–704 (2014).
96. Banu, S., Ahn, S. J., Ahn, S. K., Yoon, K. & Cho, A. Fabrication and characterization of cost-efficient CuSbS₂ thin film solar cells using hybrid inks. *Solar Energy Materials and Solar Cells* **151**, 14–23 (2016).
97. Xue, D.-J. *et al.* CuSbSe₂ as a Potential Photovoltaic Absorber Material: Studies from Theory to Experiment. *Adv Energy Mater* **5**, 1501203 (2015).
98. Welch, A. W. *et al.* CuSbSe₂ photovoltaic devices with 3% efficiency. *Applied Physics Express* **8**, 082301 (2015).
99. Welch, A. W. *et al.* Trade-Offs in Thin Film Solar Cells with Layered Chalcostibite Photovoltaic Absorbers. *Adv Energy Mater* **7**, 1601935 (2017).
100. Choi, Y. C. *et al.* Sb₂Se₃-Sensitized Inorganic–Organic Heterojunction Solar Cells Fabricated Using a Single-Source Precursor. *Angewandte Chemie International Edition* **53**, 1329–1333 (2014).
101. Leng, M. *et al.* Selenization of Sb₂Se₃ absorber layer: An efficient step to improve device performance of CdS/Sb₂Se₃ solar cells. *Appl Phys Lett* **105**, 083905 (2014).

102. Liu, X. *et al.* Improving the performance of Sb₂Se₃ thin film solar cells over 4% by controlled addition of oxygen during film deposition. *Progress in Photovoltaics: Research and Applications* **23**, 1828–1836 (2015).
103. Zhou, Y. *et al.* Thin-film Sb₂Se₃ photovoltaics with oriented one-dimensional ribbons and benign grain boundaries. *Nat Photonics* **9**, 409–415 (2015).
104. Kolay, A. *et al.* New Antimony Selenide/Nickel Oxide Photocathode Boosts the Efficiency of Graphene Quantum-Dot Co-Sensitized Solar Cells. *ACS Appl Mater Interfaces* **9**, 34915–34926 (2017).
105. Li, Z. *et al.* 9.2%-efficient core-shell structured antimony selenide nanorod array solar cells. *Nat Commun* **10**, 125 (2019).
106. Duan, Z. *et al.* Sb₂Se₃ Thin-Film Solar Cells Exceeding 10% Power Conversion Efficiency Enabled by Injection Vapor Deposition Technology. *Advanced Materials* **34**, 2202969 (2022).
107. Zhao, Y. *et al.* Regulating deposition kinetics via a novel additive-assisted chemical bath deposition technology enables fabrication of 10.57%-efficiency Sb₂Se₃ solar cells. *Energy Environ Sci* **15**, 5118–5128 (2022).
108. Itzhaik, Y., Niitsoo, O., Page, M. & Hodes, G. Sb₂Se₃-Sensitized Nanoporous TiO₂ Solar Cells. *The Journal of Physical Chemistry C* **113**, 4254–4256 (2009).
109. Nezu, S. *et al.* Light Soaking and Gas Effect on Nanocrystalline TiO₂/Sb₂Se₃/CuSCN Photovoltaic Cells following Extremely Thin Absorber Concept. *The Journal of Physical Chemistry C* **114**, 6854–6859 (2010).
110. Chang, J. A. *et al.* High-Performance Nanostructured Inorganic–Organic Heterojunction Solar Cells. *Nano Lett* **10**, 2609–2612 (2010).
111. Im, S. H. *et al.* Toward Interaction of Sensitizer and Functional Moieties in Hole-Transporting Materials for Efficient Semiconductor-Sensitized Solar Cells. *Nano Lett* **11**, 4789–4793 (2011).
112. Chang, J. A. *et al.* Panchromatic Photon-Harvesting by Hole-Conducting Materials in Inorganic–Organic Heterojunction Sensitized-Solar Cell through the Formation of Nanostructured Electron Channels. *Nano Lett* **12**, 1863–1867 (2012).
113. Choi, Y. C., Lee, D. U., Noh, J. H., Kim, E. K. & Seok, S. Il. Highly Improved Sb₂S₃ Sensitized-Inorganic–Organic Heterojunction Solar Cells and Quantification of Traps by Deep-Level Transient Spectroscopy. *Adv Funct Mater* **24**, 3587–3592 (2014).
114. Choi, Y. C. & Seok, S. Il. Efficient Sb₂S₃-Sensitized Solar Cells Via Single-Step Deposition of Sb₂S₃ Using S/Sb-Ratio-Controlled SbCl₃-Thiourea Complex Solution. *Adv Funct Mater* **25**, 2892–2898 (2015).
115. Tang, R. *et al.* Vacuum assisted solution processing for highly efficient Sb₂S₃ solar cells. *J Mater Chem A Mater* **6**, 16322–16327 (2018).
116. Nie, R., Lee, K. S., Hu, M. & Seok, S. Il. Strain Tuning via Larger Cation and Anion Codoping for Efficient and Stable Antimony-Based Solar Cells. *Advanced Science* **8**, 2002391 (2021).

117. Han, J. *et al.* Solution-Processed Sb₂S₃ Planar Thin Film Solar Cells with a Conversion Efficiency of 6.9% at an Open Circuit Voltage of 0.7 V Achieved via Surface Passivation by a SbCl₃ Interface Layer. *ACS Appl Mater Interfaces* **12**, 4970–4979 (2020).
118. Wang, S. *et al.* A Novel Multi-Sulfur Source Collaborative Chemical Bath Deposition Technology Enables 8%-Efficiency Sb₂S₃ Planar Solar Cells. *Advanced Materials* **34**, 2206242 (2022).
119. Liu, X. *et al.* Grain Engineering of Sb₂S₃ Thin Films to Enable Efficient Planar Solar Cells with High Open-Circuit Voltage. *Advanced Materials* **36**, 2305841 (2024).
120. Li, Y. *et al.* Precursor Engineering of Solution-Processed Sb₂S₃ Solar Cells. **2308895**, 1–8 (2024).
121. Messina, S., Nair, M. T. S. & Nair, P. K. Antimony Selenide Absorber Thin Films in All-Chemically Deposited Solar Cells. *J Electrochem Soc* **156**, H327 (2009).
122. Choi, Y. C. *et al.* Efficient Inorganic-Organic Heterojunction Solar Cells Employing Sb₂(S_xSe_{1-x})₃ Graded-Composition Sensitizers. *Adv Energy Mater* **4**, 1301680 (2014).
123. Wu, C. *et al.* Interfacial Engineering by Indium-Doped CdS for High Efficiency Solution Processed Sb₂(S_{1-x}Se_x)₃ Solar Cells. *ACS Appl Mater Interfaces* **11**, 3207–3213 (2019).
124. Tang, R. *et al.* Hydrothermal deposition of antimony selenosulfide thin films enables solar cells with 10% efficiency. *Nat Energy* **5**, 587–595 (2020).
125. Wang, X. *et al.* Manipulating the Electrical Properties of Sb₂(S,Se)₃ Film for High-Efficiency Solar Cell. *Adv Energy Mater* **10**, 2002341 (2020).
126. Zhao, Y. *et al.* Regulating Energy Band Alignment via Alkaline Metal Fluoride Assisted Solution Post-Treatment Enabling Sb₂(S,Se)₃ Solar Cells with 10.7% Efficiency. *Adv Energy Mater* **12**, 2103015 (2022).
127. Chen, X. *et al.* Solvent-Assisted Hydrothermal Deposition Approach for Highly-Efficient Sb₂(S,Se)₃ Thin-Film Solar Cells. *Adv Energy Mater* **13**, 2300391 (2023).